École polytechnique de Louvain

Numerical modelling of hydrofoiling sailboats

Authors: **Victor DETRY, Arnaud VAN HEMELDONCK**
Supervisors: **Philippe CHATELAIN, Matthieu DUPONCHEEL, Nicolas DOCQUIER**
Reader: **Paul FISETTE**
Academic year 2021–2022
Master [120] in Mechanical Engineering

Acknowledgments

We would like to express all our gratitude to our supervisors Pr. Philippe Chatelain, Matthieu Duponcheel and Nicolas Docquier for giving us the opportunity to work on such a thrilling topic but also for their guidance and precious advice over the year.

We also wish to thank Pr. Grégoire Winckelmans for his insights and his time reflecting with us on methods to solve the surface effect problem, which will have an important place in this writing.

Finally, we are very thankful for the relevant questions, comments and interest expressed by the whole aerodynamics team of the IMMC during the numerous plenary meetings throughout the year.

Abstract

Despite the growing interest in foiling technology with recent and increased media coverage of major sailing events and the vulgarization of foiling boards and crafts, the academic interest and the available studies on the behavior of such applications of foiling mechanics remain limited. This master thesis intends to provide a computationally fast but thorough three-dimensional numerical model of a fully hydrofoiling sailboat. The modelling of the boat's forces will be detailed, implemented into the boat's mechanical system and analyzed using a symbolic multibody approach provided by the ROBOTRAN software developed at UCLouvain. The present work is divided in two major parts.

In a first step, models for each force interacting with the boat will be presented and discussed, with a special focus on the foils as they are the major component of interest of this study. Their interaction with the free surface will be thoroughly investigated. Then, through a quasi-static equilibrium analysis with ROBOTRAN, a parametric study on simplified 2 degree of freedom simulations and a validation case based on race data with the final 5 degree of freedom model will be presented.

Keywords: Hydrofoil, sailboat, numerical simulation, free surface effect

Contents

1 Introduction **1**

2 State of the art **4**

2.1 Sailing background 4

2.2 Variety of foiling sailboats 6

2.3 Fully foiling sailboats 7

3 Model characterization **10**

3.1 Boat parameters 10

3.2 Sails aerodynamic model 13

3.2.1 Individual sails characteristics 14

3.2.2 Combined sailset characteristics 18

3.3 Foils hydrodynamic model 22

3.3.1 C_l - 2D hydrofoil 22

3.3.2 C_L - 3D hydrofoil 33

3.4 Hull 44

3.5 Rudder 44

3.6 Implementation in Robotran 45

4 Velocity prediction **47**

4.1 Robotran velocity computation 47

4.2 2 D.o.F. simulations - first stability intuitions 48

4.2.1 D.o.F. $= \phi, \alpha_{rF}$ 48

4.2.2 D.o.F. $= x, \phi$ 49

4.2.3 Modal analyses with D.o.F. $= \dot{x}, \phi$ 50

4.2.4 Varying the dimensions of the boat's main elements 51

4.3 5 D.o.F. simulations - validation of the model 61
4.3.1 Boat velocity prediction 62
4.3.2 Impact of the foil profile 66

Conclusion **67**

A Nomenclature of the sailboat **71**

B Details of computation scheme for the sails VPP **72**
B.0.1 Dimensions, standardised area and center of effort 72
B.0.2 Blanketing factors for the combined sails characteristics 73

C Pressure coefficients - "biplane image" panel method for different AoA, at h/b=0.7, NACA0012, 350panels **77**

D Biplane Lifting Line method from Section 3.3.2 **78**
D.1 Classic Lifting Line - detailed calculations 78
D.2 Biplane Lifting Line - detailed calculations 78

Nomenclature

AWA	Apparent Wind Angle
AWS	Apparent Wind Speed
PLL	Prandtl Lifting Line
TWA	True Wind Angle
TWS	True Wind Speed
VMG	Velocity Made Good
VPP	Velocity Prediction Program

α_F	Main foil angle of attack
α_{rF}	Rear foil angle of attack
δ_F	Main foil angle of tilt/cant around the x-axis of the boat
λ	Leeway angle
Fr	Froude number
V_b	Boat velocity
CE	Aerodynamic Center of Effort

θ	Heel angle
b_k, b_e	Blanketing factor

z_{CE}	Centroid of discretized sail element
A_R	Wing aspect ratio
AC75	36th America's Cup 75 feet foiling monohull
CEH	Center of Effort Height
CM	Center of Mass
D.O.F.	Degrees Of Freedom
FCS	Foil Cant System
KPP	Parasitic drag coefficient
LCP	Longitudinal Center Plane
LL	Jib luff length
MWP	Measurement Waterline Plane
P	Mainsail span
TRP	Transom Reference Plane

List of Figures

1.1 Boeing's USS High Point [left] and Admiral 350 [right]. [1][2] 1

1.2 Moth 11 feet foiling dinghy [left] and AC75 Ineos Team Britannia 75 feet foiling yacht [right]. [©NorthSails & ©C. Gregory / Ineos Team UK] 2

2.1 Main aero and hydrodynamic forces on a traditional monohull - steady state 5

2.2 Three types of common foil assistance [3] 'Dali Moustache' in blue, 'Chistera' in green, 'DSS' in pink. 6

2.3 Towing tank results on the three types of foil-assisted boat appendages. Fn = 0.35, heel = 20°, data points: λ = 0, 2, 4, 6°.[3] 7

2.4 Some of the main forces on an AC75 boat - steady state 8

3.1 Sectional view of hull and foil cant system with specified dimensions [4] . 11

3.2 AC75 hull design for computations with Solidworks 12

3.3 AC75 jib principal dimensions and terminology [4] 15

3.4 AC75 mainsail principal dimensions and terminology [4] 16

3.5 Lift and drag coefficients of the AC75 mainsail and jib as a function of AWA 18

3.6 Influence of reefing the sail set on the generated lift and drag 20

3.7 Influence of flattening the mainsail on the generated lift and drag 20

3.8 Froude number impact on the flow above the hydrofoil [5] 23

3.9 Free surface effects on lift for an uncambered thin 2D profile at an AoA as a function of F_h [6] 24

3.10 Vortex setups for both F_h regimes 24

3.11 Mirror setup for the panel code 26

3.12 Lift coefficients as a function of submergence depth obtained by the different mirror models, AoA=5°, 350panels, NACA0012 27

3.13 Lift coefficient from the mirror panel method as a function of h/c [left] and of AoA [right], 350 panels, NACA0012 28

3.14 Biplane setup for panel code . . . 29
3.15 Pressure coefficients for different submergence depths, AoA=5°, NACA0012, 350panels . . . 30
3.16 Lift coefficients as a function of submergence depth obtained by the different biplane models, AoA=5°, 250panels, NACA0012 . . . 30
3.17 Lift coefficient from the biplane panel method as a function of h/c [left] and of AoA [right], 350 panels, NACA0012 . . . 31
3.18 Biplane panel code streamlines calculation . . . 31
3.19 3D wing - Classic Lifting Line configuration . . . 33
3.20 Classic PLL setup - downstream view . . . 34
3.21 Classic PLL: circulation distribution with $\delta_F = 0^{\circ}$ and 30° . . . 35
3.22 Classic PLL: lift coefficient as a function of submergence ratio for different tilt angles . . . 36
3.23 Classic PLL: induced drag coefficient as a function of submergence ratio for different tilt angles . . . 36
3.24 3D wing - Biplane Lifting Line configuration . . . 37
3.25 Biplane PLL setup - downstream view . . . 38
3.26 Biplane PLL: circulation distribution with $\delta_F = 0^{\circ}$ and 30° . . . 39
3.27 Biplane PLL: lift coefficient as a function of submergence ratio . . . 40
3.28 Biplane PLL: induced drag coefficient as a function of submergence ratio . . . 40
3.29 Lift coefficient comparison for the different models at $\alpha_F = 5^{\circ}$, **with** $\boldsymbol{\delta_F = 0^{\circ}}$ 41
3.30 Downwash distribution for elliptical and tapered wings *out of surface effect* 42
3.31 Downwash velocity distribution for different $\frac{h}{c}$ ratios: 'Classic' vs 'Biplane' PLL . . . 43
3.32 MBSysPad visualization of the AC75 . . . 45

4.1 Top speed and drag variation as a function of main foil span . . . 52
4.2 Modes 2 and 3 of quasi-static equilibrium with varying main foil span . . . 53
4.3 Modes 4 of quasi-static equilibrium with varying main foil span . . . 53
4.4 Lift of submerged foil and rear as a function of main foil arm advance w.r.t. TRP . . . 54
4.5 Eigenvector of second mode with foil arm position at 10.5m w.r.t. TRP . . . 55
4.6 Mode 2 and mode 4 w.r.t. main foil arm advance . . . 55
4.7 Pitch and boat speed as a function of rear foil depth . . . 56
4.8 Second and fourth mode in function of rear foil depth . . . 57

4.9 Second and fourth mode as a function of foil span with TWS = 10.1 kn . . 58
4.10 Second and fourth mode as a function of foil span with TWA = 120.3 deg . 59
4.11 TWS - Race data [7] 61
4.12 Boat velocity V_b $[kn]$: Robotran prediction for different boom angles β and their envelope 62
4.13 Boat velocity V_b $[kn]$: Robotran prediction and race data for different TWS 63
4.14 Velocity made good VMG $[kn]$: Robotran prediction and race data 64
4.15 Heel [left] and pitch [right] polars: Robotran prediction 65
4.16 Heave $[m]$: Robotran prediction 65
4.17 Boat velocity V_b $[kn]$: Robotran prediction and race data 66

C.1 Pressure coefficients for different AoA, $\frac{h}{c} = 0.7$, NACA0012, 500panels . . 77

D.1 Shed vortex sheet 78

Chapter 1

Introduction

1. Context of the study

Today's marine transportation vehicles are entirely dominated by traditional displacement vessels with engine-powered propulsion systems. The use of hydrofoils on marine crafts is nowhere near a new concept, with numerous motorized high-speed marine vehicles that have had their moment of glory [8]. Boeing for instance developed some hydrofoiling military boats for the US Navy starting in the early 1960s with *USS High Point (PCH-1)* on Fig.1.1 capable of reaching 45+ knots (or 80+ kph) thanks to its 3500 horsepower turbines. Although those have had no offspring because considered too expensive to exploit, some civilian foiling vessels have also been developed since then. The most recent and largest of them all being the *Admiral 350*, a 314 tons and 38 m long high-speed craft built in 2017 and capable of transporting 350 passengers in 30 knots of boat speed, currently operating in the southern Italian islands.

Figure 1.1: Boeing's USS High Point [left] and Admiral 350 [right]. [1][2]

The use of hydrofoils on sailing boats however is a relatively recent practice with a particular thrive in the recent years because of their use on America's cup boats since the *AC72 Class catamarans* in 2013 and Vendée Globe's foil assisted *Imoca yacht* breaking the event record in 2016 by quite a margin.

An even more drastic application of this technology has been developed in the form of keel-less lift hydrofoiling monohulls, boats 'flying' over water on underwater wings. These are using 'T-shaped foils', the only type of foil generating a single-direction lift, in contrast to 'C-foils' or 'L-foils' which generate multidirectional lift. This type of foilers are indeed quite new in the sailing world with the *Moth*, a small development class of mainly home-made sailing dinghies that has been working on fully foiling boats since the early 2000s. This turned out to be a major success with considerable reduction in drag and increased speed with up to 36 knots achieved by a 2014 development model in 18-25 knots of wind [9].
More recently, renowned racing yachts using T-foils made a name for themselves with the late success of the AC75 boats, the 75 feet vessels of the 36th America's Cup which took place in 2021. These massive yachts impressed by the tremendous speeds achieved [10] even in reasonable wind conditions. Capable of flying at triple the wind speed, this boat class is the one that will be considered in this work for the development of the model.

Figure 1.2: Moth 11 feet foiling dinghy [left] and AC75 Ineos Team Britannia 75 feet foiling yacht [right]. [©NorthSails & ©C. Gregory / Ineos Team UK]

Although highlighted by those popular racing events, limited academic research can be found on this particular topic. The discipline in which those hydrofoiling sailboats are involved being extremely competitive and resource-demanding, very few data is publicly available, making the understanding of the boat's stability and dynamics a challenging task in itself.

Despite this, it should be noted that some studies [3] [11][12][13] have been conducted on foil-assisted sailboats, i.e. traditional displacement sailing vessels where a retractable foil built into the boat just above the waterline counteracts the heeling force by creating lift when the foil is projected underwater. By this means, the yacht can sail more upright, gaining in comfort and in surge force by the same token.

Concerning the topic of hydrofoils in itself, many studies can be found [14][15][16][17], some of them addressing the delicate complexity of the free surface effect on the foil's lift. Most of these studies however use complex computational methods that would be time-consuming for whole-boat dynamics modelling, and most importantly none of them are considering T-foils that are *tilted* with respect to the water surface. This parameter will turn out to be of main importance for the stability of the AC75 boat which will be considered.

2. Aim of this work

This work aims at designing a whole-boat simulation model of an AC75 class monohull flying on foils. This will be achieved through relatively basic but thorough mathematical models. Particular emphasis will be placed on the modelling of the foil's interaction with the free surface that is the water plane.

Once the models developed, a parametric analysis with 2 D.o.F simulations will be investigating the main parameters' influence on the boat stability. Lastly, a validation of the simulation model will be executed by confronting public data from the 36th America's Cup races with the stable quasistatic equilibrium positions achieved through the 5 D.o.F. simulations run by the symbolic multibody software ROBOTRAN.

Chapter 2

State of the art

2.1 Sailing background

The wind that is felt onboard a moving boat, called the apparent wind, is a combination of the true wind due to the environmental conditions and the boat speed, as depicted at the top of Fig.2.1. The heeling of the boat must also be integrated in the apparent wind in such a way that its speed and angle of incidence on the boat are:

$$\begin{aligned}
\text{AWS} &= \sqrt{(\text{TWS}\cos(\text{TWA}) + V_B)^2 + (\text{TWS}\sin(\text{TWA})\cos(\theta))^2} \\
\text{AWA} &= \text{atan}\left(\frac{\text{TWS}\sin(\text{TWA})\, cos(\theta)}{\text{TWS}\cos(\text{TWA}) + V_B}\right)
\end{aligned} \tag{2.1}$$

The aerodynamic force produced by the sails of a sailboat, applied at what will be called the aerodynamic center of effort CE, has a large component in a direction perpendicular to that from which the apparent wind is blowing. The direction of the course followed by the boat will therefore be deviated downwind of the fore-aft axis by an angle λ called the *leeway angle*. This angle will represent the angle of attack on the submerged appendages of the boat, mainly the keel, that will produce drag but also lift at the center of lateral resistance CLR. This lift is essential because it counteracts the side force, thus allowing the boat to sail upwind.

The motion in space of the rigid body that is the boat can be defined with six degrees of freedom, three translations and three rotations. The main terminology is listed in Table 2.1.

	position	angle	velocity
x_e	x	θ heel	u surge
y_e	y	ϕ pitch	v sway
z_e	z	ψ heading	w heave

Table 2.1: Motions of a boat: terminology

Fig.2.1 summarizes the main aero and hydrodynamic forces applied on a boat underway. As detailed in F. Fossati's work [18], each force should be considered through its components in a fixed frame of reference, as depicted. For instance, the aerodynamic force acting on the sails can be broken down in two components in a plane passing through CE and perpendicular to the mast: F_M being the driving force and F_H the heeling force. F_H can then also be broken down, this time in its lateral and vertical components F_{lat} & F_{vert}. The observation of the entirety of the forces depicted on Fig.2.1 makes it obvious that the boat's motion will be governed by the dynamic equilibrium of those forces.

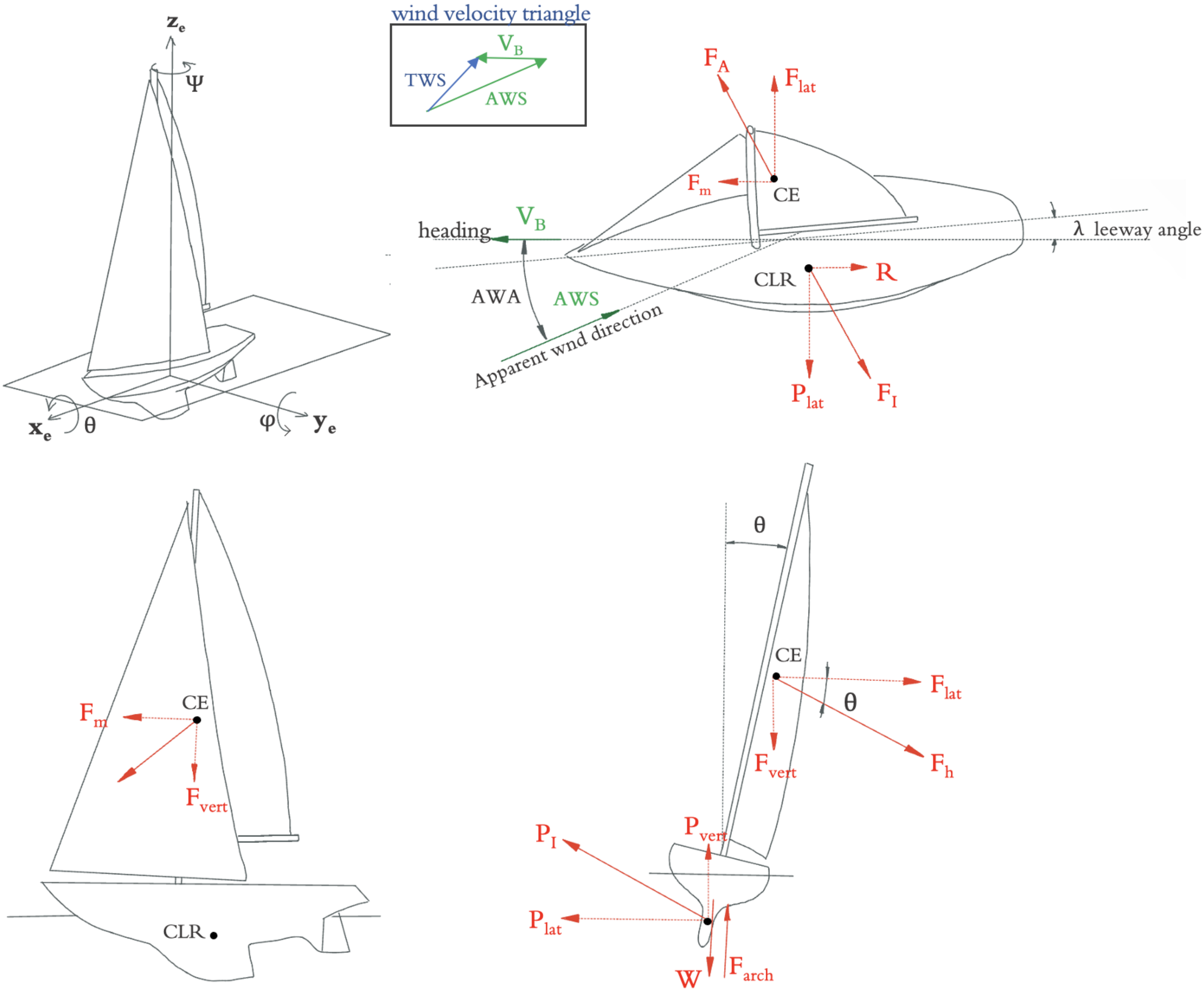

Figure 2.1: Main aero and hydrodynamic forces on a traditional monohull - steady state

2.2 Variety of foiling sailboats

Because the heeling of the boat has a negative impact on the pressure applied on the sails (see Eq.2.1), and because equilibrium is only reached thanks to the center of buoyancy moving out when the boat heels, a decrease in surge force results. Foil-assisted sailboats rely on an underwater wing structure to create more righting moment than a traditional keel boat would, hence limiting the heel. Some of them also produce side force that counteracts F_{lat}, thus improving heading by minimizing leeway. This is indeed critical for better upwind sailing.

Three main types of hydrofoils have been used on foil-assisted yachts in recent years, for instance the 'Dali Moustache' foil on the IMOCA yachts, the 'Chistera' foil on the Beneteau Figaro 3 and the 'Dynamic Stability System (DSS)' such as on the Farr Infiniti 56C yacht. Those types of foils are shown on Fig.2.2.

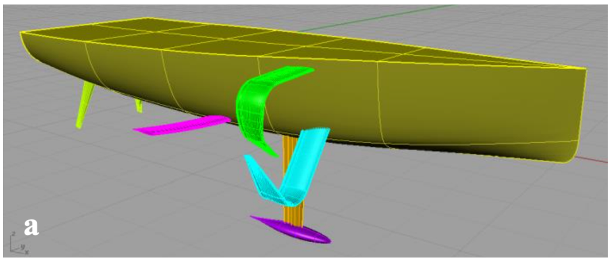

Figure 2.2: Three types of common foil assistance [3]
'Dali Moustache' in blue, 'Chistera' in green, 'DSS' in pink.

An article by Souppez et al. [3] investigates the performance of those three appendages. From towing tank results, Figure 2.3 shows on the left the total resistance R_T as a function of the side force squared $(Fh)^2$ and on the right the increase in righting moment as a function of the Froude number based on boat length $Fn = \frac{V_b}{\sqrt{g \cdot L}}$. The 'upwind sailing' line of the first plot refers to a vessel operating in TWS = 16 knots, TWA = 35°. Two placements of the Dali and Chistera foils were considered for the righting moment experiments. What can be observed is the following:

- The dali moustache foil generates way more sideforce than the others and is the only one to produce Fh without leeway (first data point). The vertical lift produced by these foils seems to have a marginal impact on the displacement of the boat. A slight impact can be seen for the 'DSS' foil at very high velocities, but the latter seems to behave quite poorly in regard to side force generation for the most used range.

- The true advantage of the 'DSS' is shown by its ability to produce the same amount of righting moment than the aft placed 'Dali' foil, up to high Fn, where negative heel and cavitation are observed (those results should therefore be taken with caution).

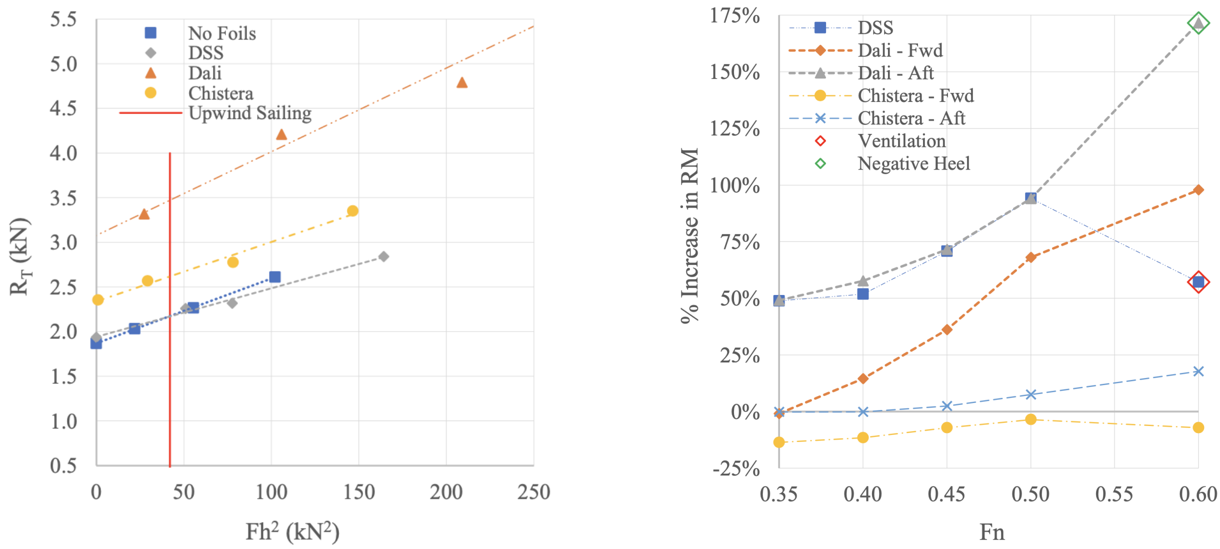

Figure 2.3: Towing tank results on the three types of foil-assisted boat appendages. Fn = 0.35, heel = 20°, data points: λ = 0, 2, 4, 6°.[3]

2.3 Fully foiling sailboats

A fully foiling -also referred to as *flying*- sailboat will add an arrow to its bow by significantly reducing overall drag, the hull being lifted out of the water when operating in regime. A schematic of the main steady state forces acting on an AC75 boat is provided in Fig.2.4.

According to which tack the boat rides on, the left or right *main foil* of the AC75 will provide the huge amount of lift necessary to overcome both the weight of the yacht and the lateral component of the sails' force. No direct setting of the angle of attack of the main foil α_F is allowed by the America's Cup regulations, meaning that the control of the boat's ride height and general equilibrium will only be managed through the pitching up or down of the whole boat with the help of the rear foil's incidence α_{rF}. In practice, a flap is also mounted on the main foils, in order to ease take-off at low speeds. Such a manoeuver would also be carried out with both foils down in the water.

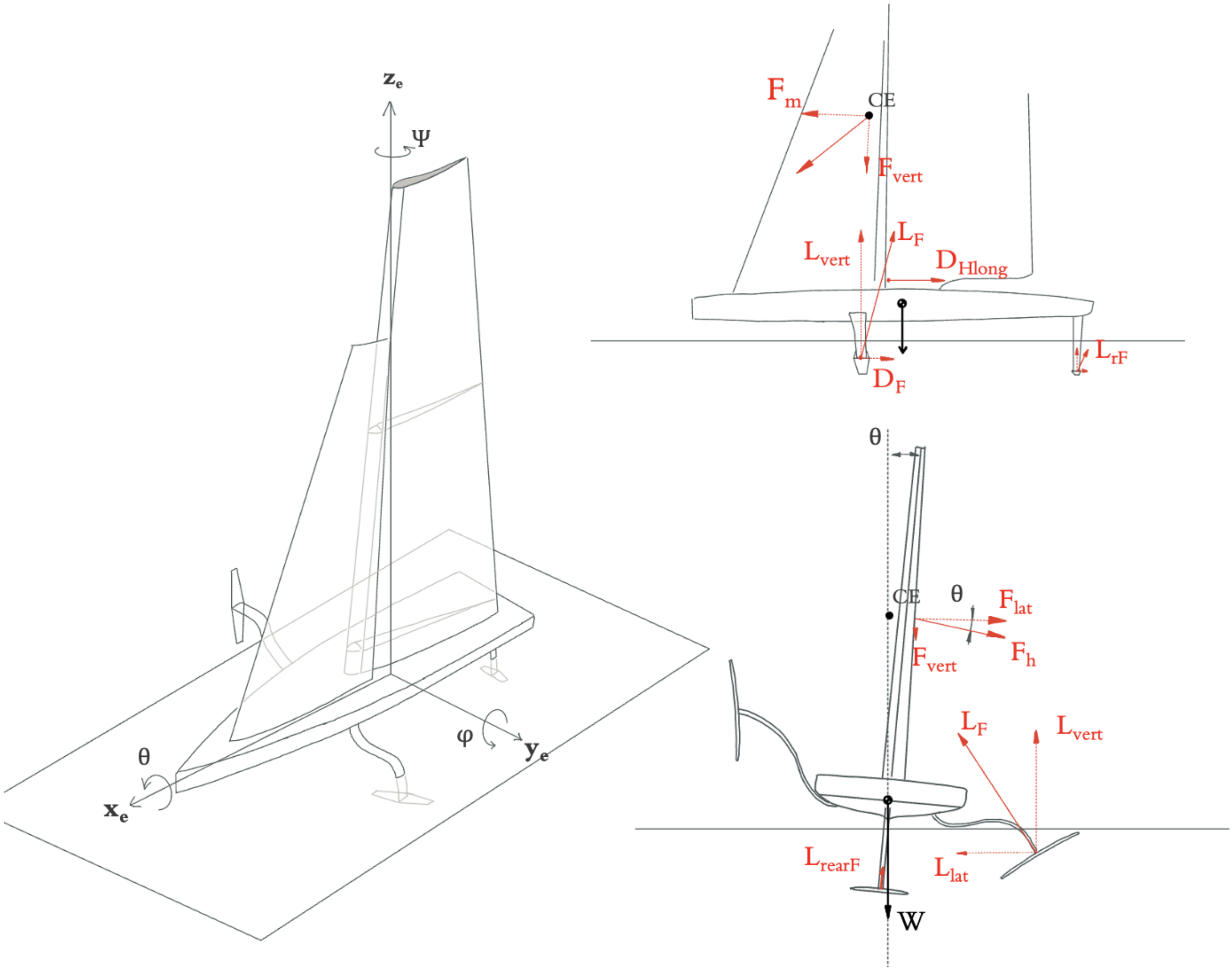

Figure 2.4: Some of the main forces on an AC75 boat - steady state

Performance prediction methods

The issue of predicting the performance of a sailing boat dates back to the middle of the 20th century, when the first methods for forecasting V_B were offered. Velocity prediction programs (VPP in short) are mainly composed of two key elements: a mathematical model of the boat and an algorithm solving the equations of motion, for which the primary output is a polar plot of the boat's maximum velocity as a function of TWS and TWA. Most of the basic VPPs allow for the calculation of boat speed and heel angle once the TWS and TWA have been assigned. Yaw and pitch are usually ignored. Yet, much more can be achieved by some modern and cutting-edge codes that are mainly used for racing boat research, with for example the calculation of a yacht unsteady responses such as tacking [19] or the impact of wave induced drag [6].

The velocity predictions intended to be achieved here will necessarily require the resolution of more equations of motion than only the one for the forward motion and the heel. The pitching motion will surely be critical due to its dramatic impact on the foils AoA, but the heave motion (in the z-direction) might also have an influence of some significance on the lift generated by the foils, as those will progressively reach the water boundary. This effect will be investigated in a next part of this chapter.
The results of the velocity prediction will be used to identify key parameters in the optimization process of the boat, up to reaching the maximum velocity achievable.

Chapter 3

Model characterization

An implementation of the different force models that will be used in the later simulations is proposed and discussed in this chapter. An introducing section will first describe the main parameters of the chosen competition foiling sailboat, some for which freedom is allowed by the racing regulations, others which are strictly imposed.
Particular attention will be paid to the model of the foils' force since being the main and most sensitive component of this whole study.
To close this chapter, the implementation of these forces in ROBOTRAN will be detailed.

3.1 Boat parameters

While some dimensions and boat parameters are settled by the America's Cup teams, others are bounded or strictly fixed by the Class rules [4]. This section will browse through the most important of these specifications.

Main elements: dimensions and properties

On Table 3.1 are listed some of the boat's main requirements. Fig.3.1 depicts a precise example of typical constraints fixed by the regulations, with the case of the foil assembly and the actual area in which it should lie.

	dimension [m]
Hull length	20.6 - 20.7
Mast height	26.5
Mainsail foot & head girth	7-7.4 & 2.6-3.6
Foil span	$\geq$ 2.942
	position [m]
Mast (provided)	x= 9.15
...	

	mass (kg)	center of mass (x;z) [m]
Yacht assembly	6508-6538	(8.855-9.385 ; <0.627)
Foil wing	1378-1385	(9.95-12 ; /) ; /)
Foil arm (provided)	464	/
FCS (provided)	343.5	(10.5-11.8 ; 0.25)
Sails	<145	/
Crew	1114-1154	/
...		

Table 3.1: Main imposed specifications of the AC75 [4]

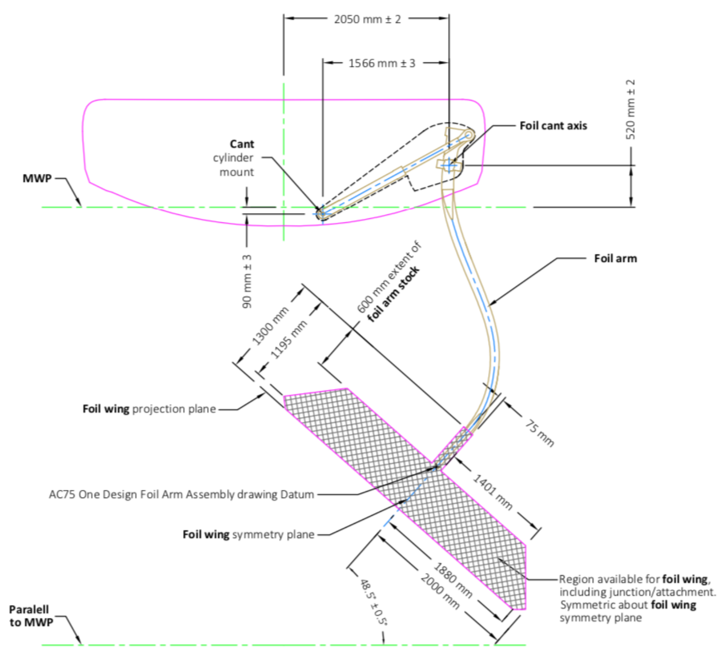

Figure 3.1: Sectional view of hull and foil cant system with specified dimensions [4]

Arbitrary choices had to be made and, in order to be as realistic as possible, some were established based on what could be found about the racing models. Such an example would be the boat's hull design. A three-dimensional CAD model has been drawn (Fig.3.2) based on pictures and regulated dimensions, and the mass, the center of mass and the inertia matrix were then computed.

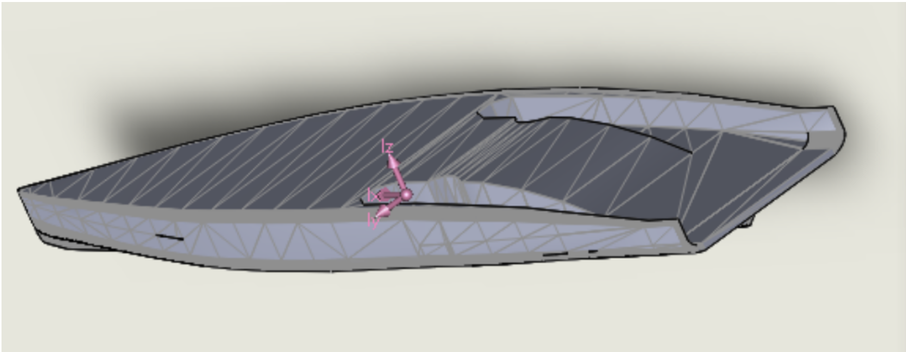

Figure 3.2: AC75 hull design for computations with SOLIDWORKS

Some of the elements' positions were of course the result of a later evaluation, based on first equilibrium points' calculations, once the boat was fully modelled. For instance, a first foil angle of attack α_F was chosen and a first equilibrium was computed at a quite common wind condition similar to what the boat would experience during a race. This computation was chosen so that the boat would ride horizontally without any rear foil action therefore with $\alpha_{rF} = 0°$. This fixed for instance the longitudinal position of the main foils. Adjustments naturally had to be made in order to comply with regulations and to reach the best overall performance that will be presented in Section 4.3.1.

3.2 Sails aerodynamic model

Once assigned the environmental conditions of true wind and a set of *first attempt* values for the boat motion variables (such as the boat velocity V_B, the heel θ, the pitch ϕ,..), the aerodynamic model will generate the forces in terms of lift and drag produced by the sail plan. From the values of AWS and AWA (Eq.2.1), the drag and lift developed are computed as traditional aerodynamic forces:

$$L_A = \frac{1}{2}\,\rho_{air}\,C_L(\alpha)\,S_{sails}\,AWS^2 \tag{3.1}$$

$$D_A = \frac{1}{2}\,\rho_{air}\,C_D(\alpha)\,S_{sails}\,AWS^2 \tag{3.2}$$

with α the apparent wind *seen by the sails*, i.e. considering a possible boom angle, as will be discussed in Section 4.
From this, the surge and heel forces will be computed as:

$$F_M = L_A\,sin(\alpha) - D_A\,cos(\alpha) \tag{3.3}$$

$$F_H = L_A\,cos(\alpha) + D_A\,sin(\alpha) \tag{3.4}$$

Most VPPs' aerodynamic models consider different combinations of the sails available on the boat, also known as *sailsets.* A database with the aerodynamic coefficients for each sailset is therefore needed. What is also needed is the position of the center of effort CE. While top-edge VPPs will use wind tunnel testing or CFD, most commercial ones use a geometrical estimate and take into account a variation in height when the sails are trimmed.
The model for the center of effort height, the lift and the drag coefficients with control parameters known as *reef* and *flat* to reproduce any depowering of the sail plan will be implemented as described by the 2021 ORC International aerodynamic model[20]. This model is based on the historically known Kerwin model[21]. The main inputs are the geometry of the sail as well as the AWA and AWS of the boat. From those inputs it retrieves a lift coefficient, a parasitic drag coefficient associated with the skin friction of the sail and an induced drag coefficient which is a direct consequence of the 3-D flow over a wing with finite span. The model gives the other essential output, i.e. the center of effort of the resulting wind force on the sail. This parameter will be critical to model the heeling of the sailboat. Finally, a computation scheme is proposed to unite the sails into *sailsets.* As far as the boat developed in this work is concerned, only a mainsail and a jib interaction will be computed. It is interesting to note that, because the model does not compute any rotational moment on the sails, the force must then be located fictitiously forward of the mainsail.

A word on the ORC - Offshore Racing Congress

In the beginning of the 20th century, several organisations emerged in the United States and Great Britain trying to come up with a set of rules to be used for offshore racing. These committees, although having similar guidelines, diverged on some points which impacted international racing. After World War II, when offshore racing resumed, these divergences became more and more predominant as international racing was promoted. The ORCC, Offshore Rules Coordinating Committee, was born in 1961 by a merge of different committees, later renamed to ORC (Offshore Racing Congress). This international body continues up to this day to govern the general principles and the operational aspects of the offshore *rating* rules, giving strict regulations on measurement as well as best practices to determine certain key parameters of a sailboat. [22].

3.2.1 Individual sails characteristics

Dimensions, center of effort and twin-skin mainsail

In order to compute the reference sail area, a trapezoidal discretization is carried out, with strict regulations on the measurement points and methods. More details about this discretization and those computations can be found in Appendix B.

The center of effort height can be calculated as the centroïd of area of the projected mainsail trapezoïd areas. One can note a correction term added to the main sail center of effort, mainly due to a wish of continuity throughout the model's evolution.

$$CEH_{mainsail} = \frac{\Sigma_i A_i \cdot zc_i}{\Sigma_i A_i} + 0.024 \cdot P \tag{3.5}$$

$$CEH_{jib} = \frac{\Sigma_i A_i \cdot zc_i}{\Sigma_i A_i} \tag{3.6}$$

with zc_i, the height above the P base of the centroïd of each trapezoïd.

Fig.3.3 and 3.4 show the main geometries and measures of the head and main sails of the AC75, such as stated in the rules. These are the ones used to develop the model below. At this point, it is useful to mention that the mainsail of the AC75 is a *twin-skin* sail. By having two mainsails set on the straight edge of a rotating D-section mast, a trimming of the leeward sail to a larger depth than the windward sail can be achieved in order to form a very powerful vertical foil able to produce sufficient surge force for the lift-off phase. The rotating mast, for its part, will ensure better flow behaviour at the leading edge for low AWA. Additionally, this particular mainsail is used in the absence of a high boom, therefore lowering the mainsail as close to the hull's deck as possible. This can be observed and compared to a traditional boom setup on Fig.1.2 of the Introduction. Envisioned in order to block the airflow from the low to high pressure side of the sail, this will improve its aerodynamic abilities and lower its center of effort height.

These cutting-edge technologies are what allow the boat to start flying but also to reach very low AWA once on its foils, therefore going upwind like no other yacht can.

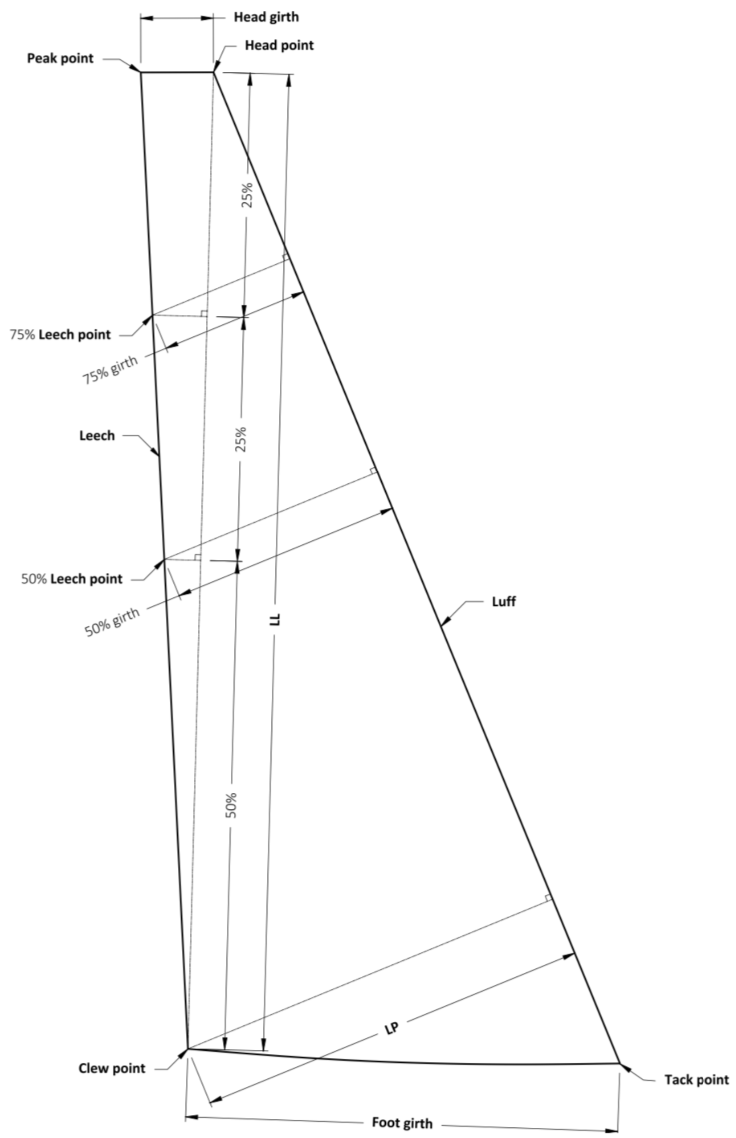

Figure 3.3: AC75 jib principal dimensions and terminology [4]

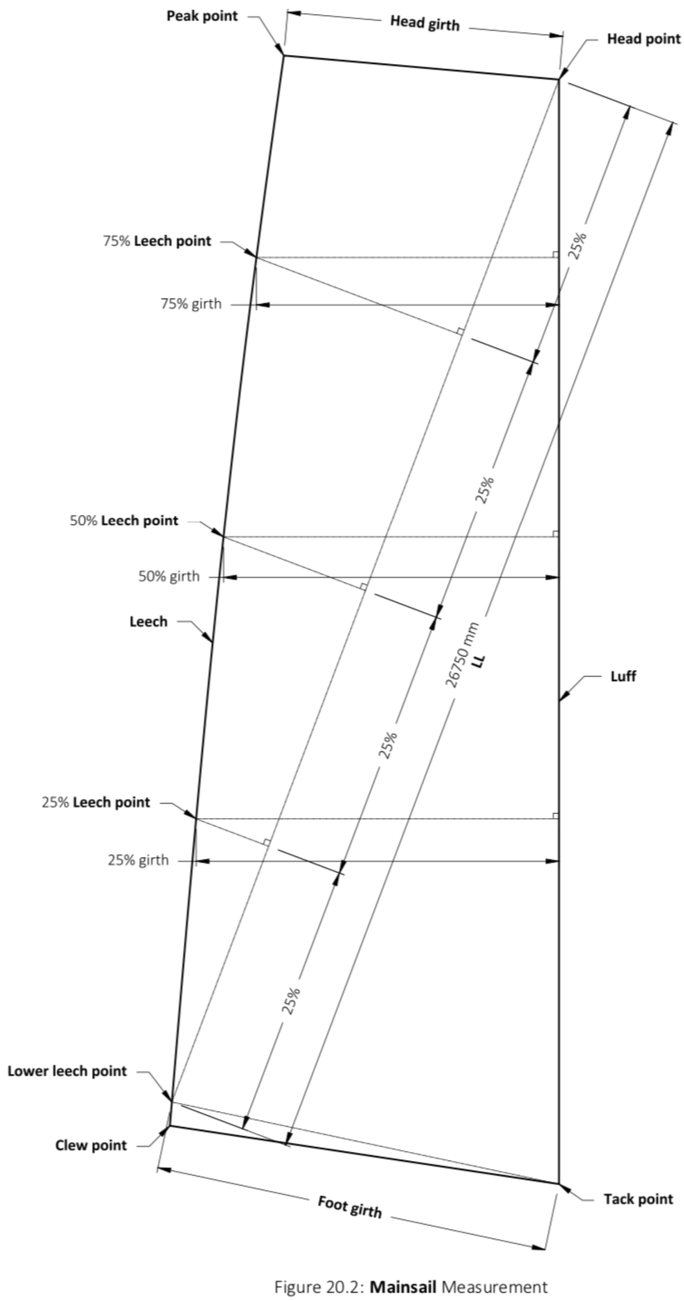

Figure 3.4: AC75 mainsail principal dimensions and terminology [4]

Lift, parasitic drag and induced drag coefficients

The values of lift and drag coefficients C_L and C_D are tabulated in the *ORC VPP documentation* [20] from years of experimental and numerical testing. Due to a lack of available data on the aerodynamic performance of the AC75 twin-skinned sail, this model will use a modified aero-coefficient curve. Based on public statements of Emirates Team New Zealand sail designer, Burns Fallow, as well as on a CFD analysis of high performance sails carried out by CARAHER ET AL.[23], a peak C_L of at least 2.2 can be expected as soon as AWA$\approx$ 20°. This of course remains one of the major assumptions of the boat model developed here, and must therefore be borne in mind throughout the analysis.

A fit was therefore applied on the ORC coefficients in order to better act for the twin-skin mainsail benefits in a certain range of AWA. The adapted values are listed and compared to a standard one-cloth mainsail in Table 3.2.

$\alpha[deg]$	$C_L[-]$ twin-skin	$C_L[-]$ single skin	$C_{D,0}[-]$
0	0.00000	0.00000	0.03448
7	**1.46215**	0.94828	0.01724
9	**1.75458**	1.13793	0.01466
12	**1.92737**	1.25000	0.01466
28	**2.20000**	1.42681	0.02586
60	**1.66900**	1.38319	0.11302
90	1.26724	1.26724	0.382508
120	0.93103	0.93103	0.96888
150	0.38793	0.38793	1.31578
180	-0.11207	-0.11207	1.34483

Table 3.2: C_L and $C_{D,0}$ of a triangular sail for various angles of attack

Table 3.3 displays the jib coefficients that have been chosen to be the ones prescribed by the ORC due to the classic design of the AC75's jib sail.

$\alpha[deg]$	$C_L[-]$	$C_{D,0}[-]$
7	0.00000	0.05000
15	1.10000	0.03200
20	1.47500	0.03100
27	1.50000	0.03700
50	1.45000	0.25000
60	1.25000	0.35000
100	0.40000	0.73000
150	0.00000	0.95000
180	-0.10000	0.90000

Table 3.3: C_L and C_D of a jib for various angles of attack

A synthesis of these coefficients' behaviour is available on Fig.3.5, where one can see a much higher lift achieved by the mainsail than by the jib compared to what would normally be observed on traditional sailsets. Once again, this remains a strong assumption of this model, which is however believed to be reasonably accurate.

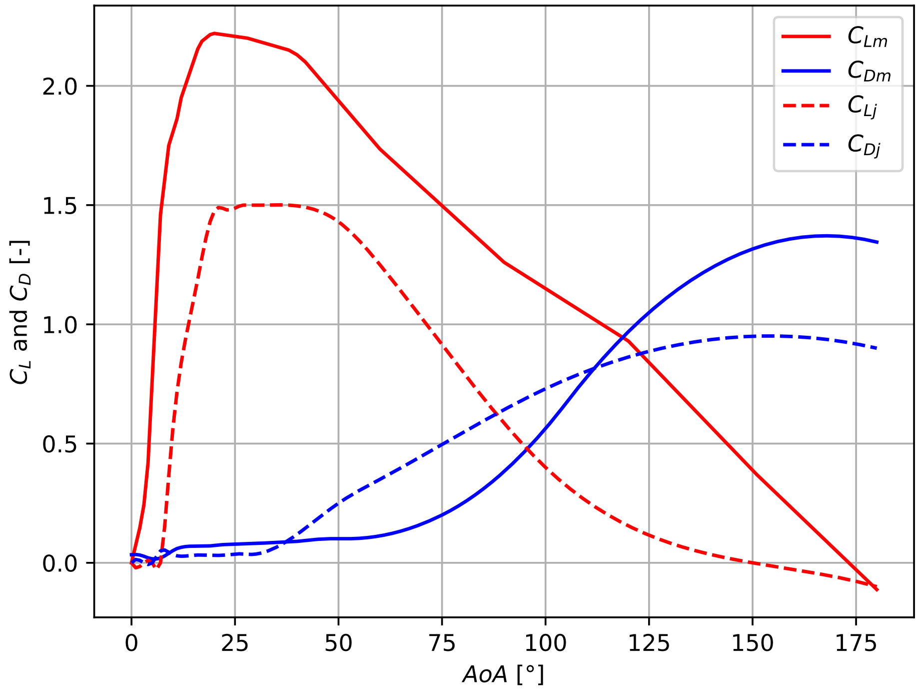

Figure 3.5: Lift and drag coefficients of the AC75 mainsail and jib as a function of AWA

3.2.2 Combined sailset characteristics

Now that the aerodynamics of each sail have been individually computed, a computation scheme is needed to determine the combined sails characteristics based on a weighting of the individual sails coefficient with the help of blanketing factors. Those blanketing factors depend on the AWA and depict the overlap interaction between the main sail and the jib. They are discussed in further details in Appendix B. All individual sail coefficients weighted by the adequate blanketing factor are then summed up and normalised by the total reference sail area $A_{ref} = A_{ref,mainsail} + A_{ref,jib}$:

$$C_{L,max} = \sum_i C_{L,i} \cdot b_{k,i} \cdot \frac{A_i}{A_{ref}} \tag{3.7}$$

$$C_{D,0,max} = \sum_i C_{D,0,i} \cdot b_{k,i} \cdot \frac{A_i}{A_{ref}} \tag{3.8}$$

The center of effort height of the total sailplan is also weighted with a similar scheme:

$$Z_{ce,tot} = \sum_i \frac{A_i \cdot Z_{ce,i}\sqrt{C_{L,i}^2 + C_{D,0,i}^2} \cdot bk_i}{A_{ref} \cdot \sqrt{C_{L,tot}^2 + C_{D,0,tot}^2}} \tag{3.9}$$

In order to compute the induced drag component, an efficiency coefficient is derived. This efficiency coefficient is such that, when multiplied by the combined lift coefficient squared, it yields the combined induced drag of the sails. This efficiency is comprised of a two-dimensional part that describes the increase of viscous drag occurring as the sail gains lift and the *induced drag* that depends on the effective rig height (a function of the mainsail roach, the relative positions of the mainsail head and the jib head, the possible overlap of the headsail and the depowering).

Finally, the total lift and drag coefficients are computed as follows:

$$C_{L,tot} = flat \cdot C_{L,max} \tag{3.10}$$

$$C_{D,tot} = C_{D,0,max} \cdot [\, flat \cdot fcdmult \cdot fcdj + (1 - fcdj)] + \textit{coeff} \cdot C_{L,max}^2 \cdot flat^2 \cdot fcdmult \tag{3.11}$$

where *flat* characterizes a reduction in the camber of the sails in such a way that the lift is proportionally reduced from the maximum lift available, *coeff* is the efficiency coefficient, *fcdj* is the fraction of parasitic drag due to the jib and *fcdmult* is an empirical coefficient. Again, further explanations and details on those parameters can be found in Appendix B.

Control of the sails aerodynamic behaviour

Two very crucial parameters are used in this model. Indeed, in strong winds the boat might be subjected to too high heeling moments. In order to avoid capsizing, the skippers can tune the span or increase the camber of the sails to reduce their wind load and thus the heeling moment of the boat. In order to simulate the decrease of heeling force by the skippers, trimming and changing sails, *flat* and *reef* parameters will be used in the model.

Reef: The most basic instinct for power reduction would be to decrease the *area* of the sail up to desired equilibrium of the boat. In case of strong winds, the jib will be reefed first. Is is only when the jib is fully folded that the reefing of the mainsail begins. A special reef parameter will therefore be used in the model where the range [0,1] refers to the reefing of the mainsail and the range [1,2] to the reefing of the jib. Although being a simple concept, it is in practice difficult to achieve during racing conditions, hence rarely used.

Flat: In light wind, a *cambered* sail with lots of shape is the fastest, but as the wind speed increases, the sail needs to be flattened to reduce its power. This will thus stabilize the heeling of the boat just as reefing would. It is important to note that flat = 1 does not mean that the sail is perfectly flat but that the camber yields the maximum lift force. The flattening of the mainsail is controlled by the skipper, who can choose to electronically actuate the battens on the sail. In order to reflect that a depowering of the sails lowers the center of effort height, a "twist function" is introduced in the model, relating Z_{CE} to the amount of *flat* used.

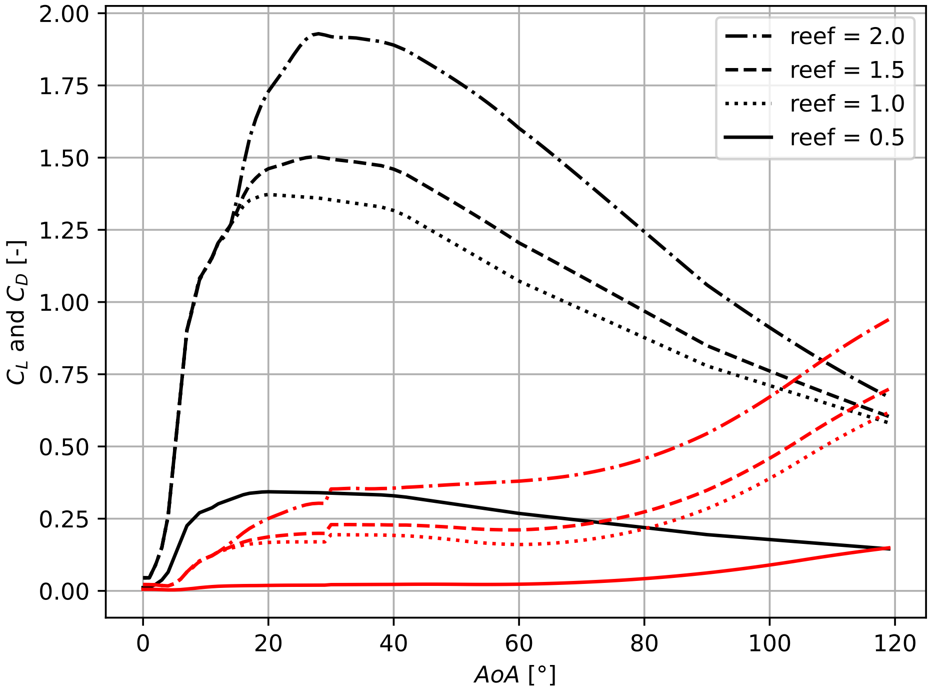

Figure 3.6: Influence of reefing the sail set on the generated lift and drag

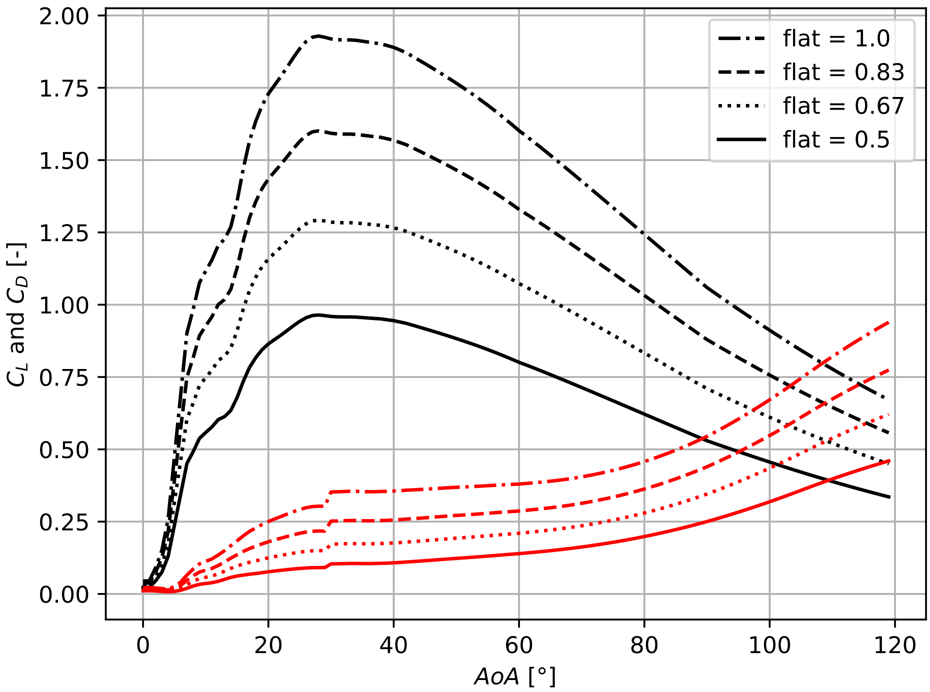

Figure 3.7: Influence of flattening the mainsail on the generated lift and drag

The previous figures show that reefing has a strongly non-linear effect on the aero-coefficients of the sail set. One can clearly see that, as long as only the jib is reefed ($1 < reef < 2$), the general lift and drag are slightly decreased. However, when the mainsail is reefed, a strong loss of lift and drag is observed, thus greatly reducing the heeling moment.

Flattening, on the other hand, has a highly linear effect on the lift coefficient of the sail set. Even though the minimum flat does not yield as strong results as the minimum reef, it still halves the generated lift and thus greatly reduces the heeling moment.

3.3 Foils hydrodynamic model

Although having dimensional regulations as detailed in the first section of this chapter, the foils of the AC75 are left relatively free to the imagination of the teams taking part in the competition. With special attention paid to these regulations [4], the configurations chosen in order to compute the lift and drag with relatively basic methods are summarized in Table 3.4.

Main foils	
profile	NACA0012 (GA(W)-1 will be discussed later)
planform	tapered
chord c	$c_{min} = 0.2$[m], $c_{max} = 0.5$[m]
span b	4 [m]
A_R	11.43
	no sweep, no dihedral
Back foil	
profile	NACA0012
planform	tapered
chord c	$c_{min} = 0.125$[m], $c_{max} = 0.25$[m]
span b	2.1 [m]
A_R	11.20
	no sweep, no dihedral

Table 3.4: Foils characteristics chosen for the model

This section will be divided in two main segments. The first will investigate the computation of lift for a two-dimensional potential flow over the chosen airfoil, with a first insight on how to model the effect that the foil will face when approaching the free surface. The second segment will investigate the lift computation for the three-dimensional wing with two different applications of Prandtl Lifting Line theory to once again take the surface effect into account. It is of importance to note that the specificity of the model developed in this chapter resides in the fact that the AC75's main foils will approach the surface not parallel to it but at an angle δ_F in order for the boat to create anti-drift force.

3.3.1 C_l - 2D hydrofoil

Airfoils and hydrofoils operate in fluids which differ in properties - mainly the density ρ and the viscosity μ - that are treated by the dimensionless Reynolds number. While the airfoil generally operates in an infinite medium, it can at some point operate close to a rigid boundary in what is called a "ground effect". The hydrofoil on the other hand operates mainly, by design, close to a boundary of another type: a free boundary.
To better understand problems arising from the hydrofoil operating close to a free surface, Parkin *et al.*[5] conducted an experiment exhibiting that two main flow regimes exist on a

two-dimensional hydrofoil, depending on whether that the Froude number based on profile chord length $Fr_c = \frac{U_\infty}{\sqrt{gc}}$ is either low or high.

Figure 3.8(a) shows that for $Fr_c \to 0$, the surface is broken by gravity waves or hydraulic jumps. Indeed, at very low submergence depth, the flow above the rear end of the upper foil surface can be processed as being in a slightly inclined open channel where the renowned channel effects such as these hydraulics jumps, may appear.
Figure 3.8(b), where $Fr_c \to \infty$, shows that the flow is smooth over the upper surface and no discontinuity occurs on the water plane.

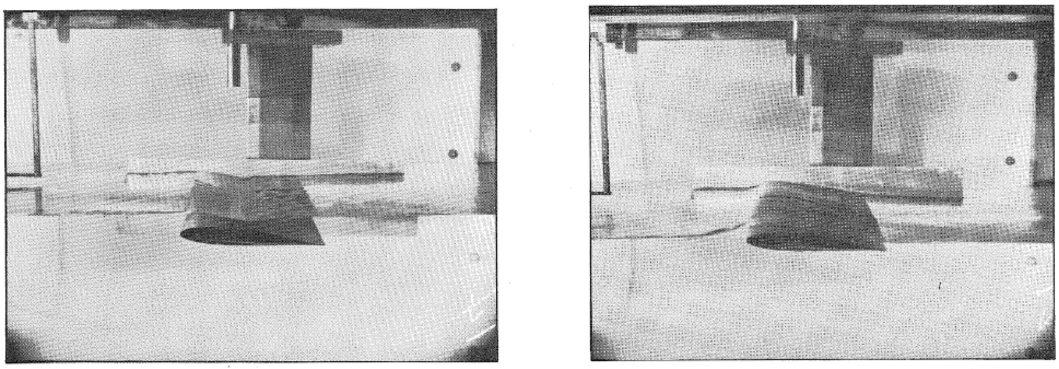

(a) Low Froude number. (b) High Froude number.

Figure 3.8: Froude number impact on the flow above the hydrofoil [5]

The study of Froude number influence on the lift coefficient of a hydrofoil in surface proximity deserves an analysis of its own and was conducted in Faltinsen's work [6]. Fig. 3.9 shows for different values of depth to chord ratio $\frac{h}{c}$ the lift ratio $\frac{C_l(h/c)}{C_l(h/c=\infty)}$ as a function of *submergence* Froude number $Fr_h = \frac{U_\infty}{\sqrt{gh}}$.
These results, obtained previously by Hough&Moran, indicate that at $Fr_h < 10$, lift generally decreases and reaches a minimum that depends on $\frac{h}{c}$ before adopting an antagonist behaviour for very low Froude numbers where the lift ratio becomes larger than unity.
It is also shown that running at a sufficiently large Froude number is practically equivalent to operation at infinite Froude.

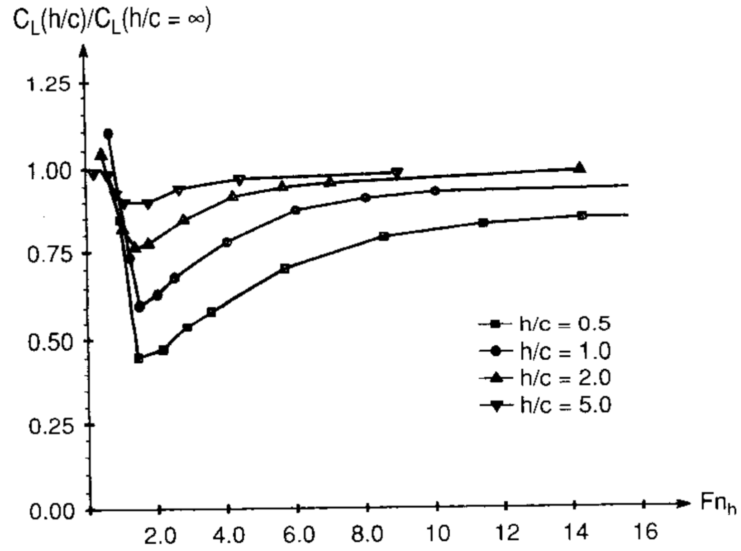

Figure 3.9: Free surface effects on lift for an uncambered thin 2D profile at an AoA as a function of F_h [6]

Hence it is concluded that again, two limiting flow regimes exist, each having opposite effects on the foils' lift coefficient.
In the limiting case $Fr_h \rightarrow 0$, the surface acts as a rigid wall and an increase in lift is noted. The problem is therefore similar to the well-known "airfoil in ground effect", where the lift in an infinite fluid is influenced by a "mirror" image system. To satisfy the rigid surface condition, the mirror vortex has an opposite sign as depicted on Fig. 3.10(a).

In the second limiting case $Fr_h \rightarrow \infty$, a similar analysis is conducted with the difference that the image vortex now has a similar sign as the foil vortex, as shown on Fig. 3.10(b).

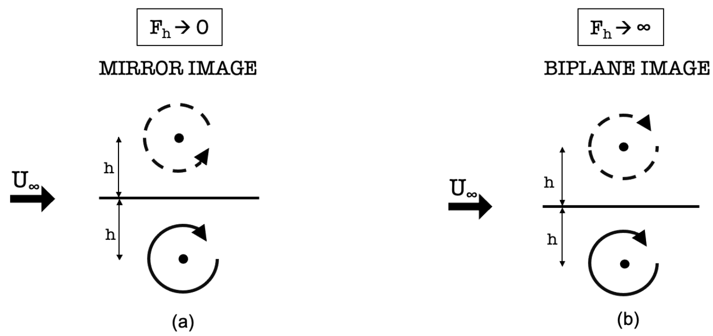

Figure 3.10: Vortex setups for both F_h regimes

In what follows, both regimes will be modelled firstly with a *Simplified* quarter chord single vortex model (A) and secondly with a *Linear Vortex Panel method* (B) as stated in [24].

(A) Simplified single vortex models

(A.a) $F_h \to 0$: The "mirror image"

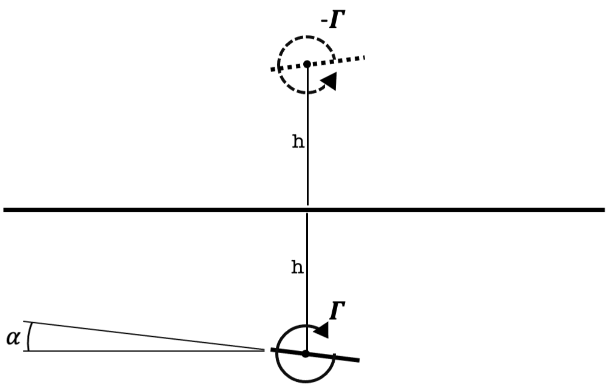

(A.b) $F_h \to \infty$: The "biplane image"

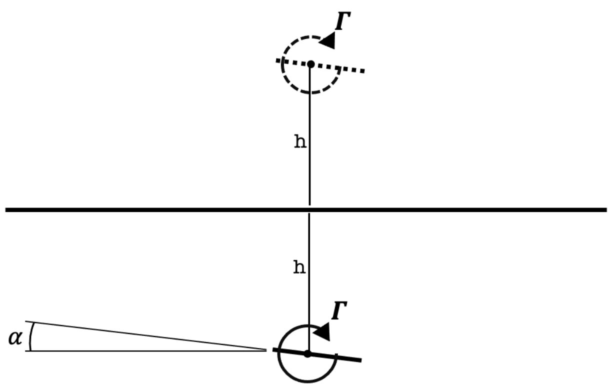

From the lift coefficient of a thin airfoil with a small angle of attack α: $\quad C_l \approx 2\pi\alpha$,
the effective velocity vector due to the image vortex is obtained as:

$$U_e = U_\infty + \frac{\Gamma}{2\pi \cdot 2h} = U_\infty + \frac{\Gamma}{4\pi h}$$

$$U_e = U_\infty - \frac{\Gamma}{2\pi \cdot 2h} = U_\infty - \frac{\Gamma}{4\pi h}$$

With $l = \rho\, U_e\, \Gamma$ and $l = \frac{1}{2}\, \rho\, U_e^2\, c\, C_l$, it results that:

$$\Gamma = U_e\, c\, \pi\, \alpha$$

Injecting that back into the equation for U_e gets:

$$\begin{aligned} U_e &= U_\infty + \frac{U_e\, c\, \pi\, \alpha}{4\pi h} \\ &= \frac{U_\infty}{(1 - \alpha \frac{c}{4h})} \end{aligned}$$

$$\begin{aligned} U_e &= U_\infty - \frac{U_e\, c\, \pi\, \alpha}{4\pi h} \\ &= \frac{U_\infty}{(1 + \alpha \frac{c}{4h})} \end{aligned}$$

The lift coefficient of the hydrofoil is obtained for both regimes:

$$\begin{aligned} C_l &= \frac{l}{\frac{1}{2}\, \rho\, U_\infty^2\, c} \\ &= \frac{2\pi\, \alpha}{(1 - \frac{\alpha\, c}{4h})^2} \end{aligned} \tag{3.12}$$

$$\begin{aligned} C_l &= \frac{l}{\frac{1}{2}\, \rho\, U_\infty^2\, c} \\ &= \frac{2\pi\, \alpha}{(1 + \frac{\alpha\, c}{4h})^2} \end{aligned} \tag{3.13}$$

(B) Linear Vortex Panel methods

This second method inspired by [24] will consist in solving both regimes by the means of a discretization of the real NACA0012 profile in *n* vortex panels with a linear distribution of circulation per unit length $\gamma(x)$. $\gamma(x)$ effectively contains all the vorticity within the boundary layer since $\gamma(x) = \int_0^{\delta(x)} \omega(x,y)\, dy$ where $\delta(x)$ is the effective boundary layer thickness and $\omega = -\frac{\partial u}{\partial y}$. It therefore follows that $\gamma(x) = -u_e(x)$.
In the limit of a fairly high Reynolds number, $\delta(x) \to 0$ and the boundary layer therefore becomes an "infinitely thin vortex sheet", still with $\gamma(x) = -u_e(x)$. This composes the basis of the *panel method* used below.

The abscissa chosen for the discretization will be such that more panels are located at the leading and trailing edges. The velocity beneath panel *i* is induced by panel *j* and *by its image*, and is computed with the integration of Biot-Savart law. The condition that the normal velocity at the center of each panel must be zero provides *n* linear equations. To close the problem, Kutta-Joukoswki's condition constraining the velocity vector just after the trailing edge to be regular is written as $\gamma_1 + \gamma_n = 0$. In other words, the total vorticity flux in the wake is zero. Solving this system "in the least square error sense" gives the circulation distribution along s, the distance coordinate measured on the airfoil.

(B.a) $F_h \to 0$: Numerical solution to the "mirror image" problem

Figure 3.11 describes the "image mirror hydrofoil" panel method developed. It should be noted that it differs from traditional "aircraft wing in ground effect" because of the angle of attack at which the profile approaches the 'ground'.
Once the system of $n+1$ equations solved, the lift coefficient can be easily found on the basis of the force exerted by the fluid on the ground:

$$l = \int_{-\infty}^{\infty} (p - p_\infty)\, dx$$
$$C_l = \frac{l}{\frac{1}{2}\rho U_\infty^2\, c} \tag{3.14}$$

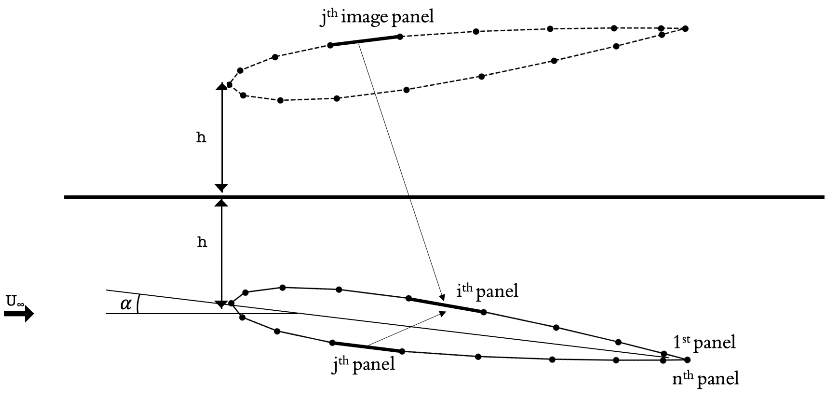

Figure 3.11: Mirror setup for the panel code

Figure 3.12 shows the results of both methods discussed here above. The panel method was computed with 350 panels in order to reach sufficient accuracy.

One can see that the simplified model predicts a similar tendency although offsetted by quite a margin. When $\frac{h}{c} \rightarrow 0$, the simplified model tends to infinity. It is also interesting to note that the influence of the surface for $\frac{h}{c} > 1$ is insignificant, although being the main range associated with the $Fr_h \rightarrow 0$ regime of a practical hydrofoil. Fig. 3.13 shows the impact of the AoA on the surface effect predicted by the "mirror" image panel method. Looking at the left graph from right to left, the increase rate of C_l with the surface approach decreases with α having up to 50% and 30% increase in lift for angles of attack of respectively 2 and 10° when reaching the minimal submergence depth.

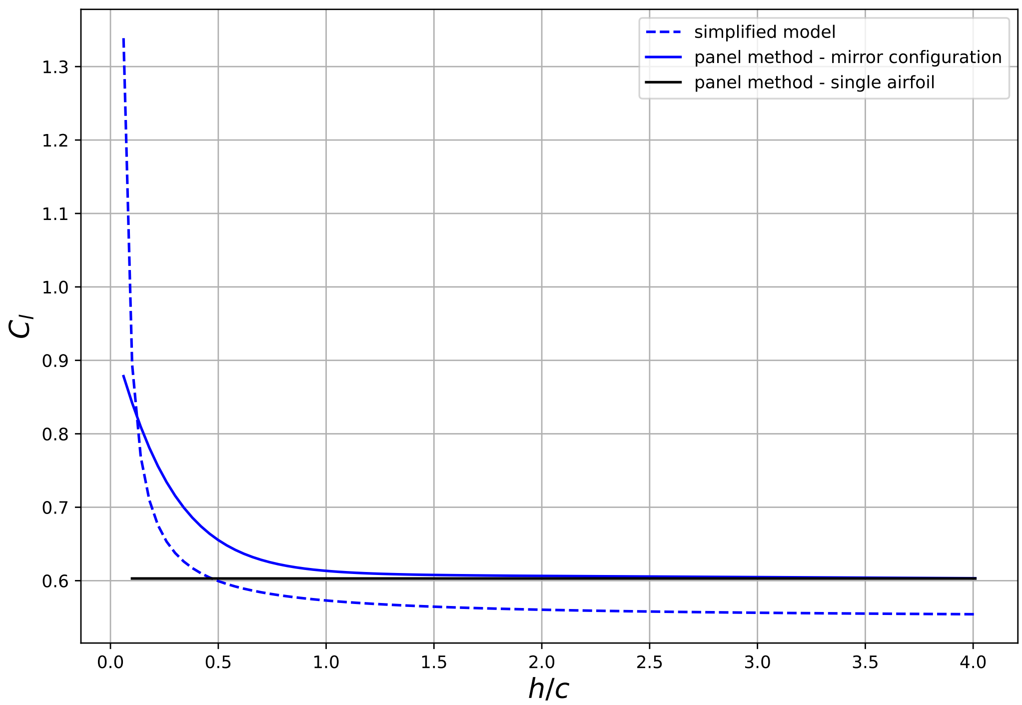

Figure 3.12: Lift coefficients as a function of submergence depth obtained by the different mirror models, AoA=5°, 350panels, NACA0012

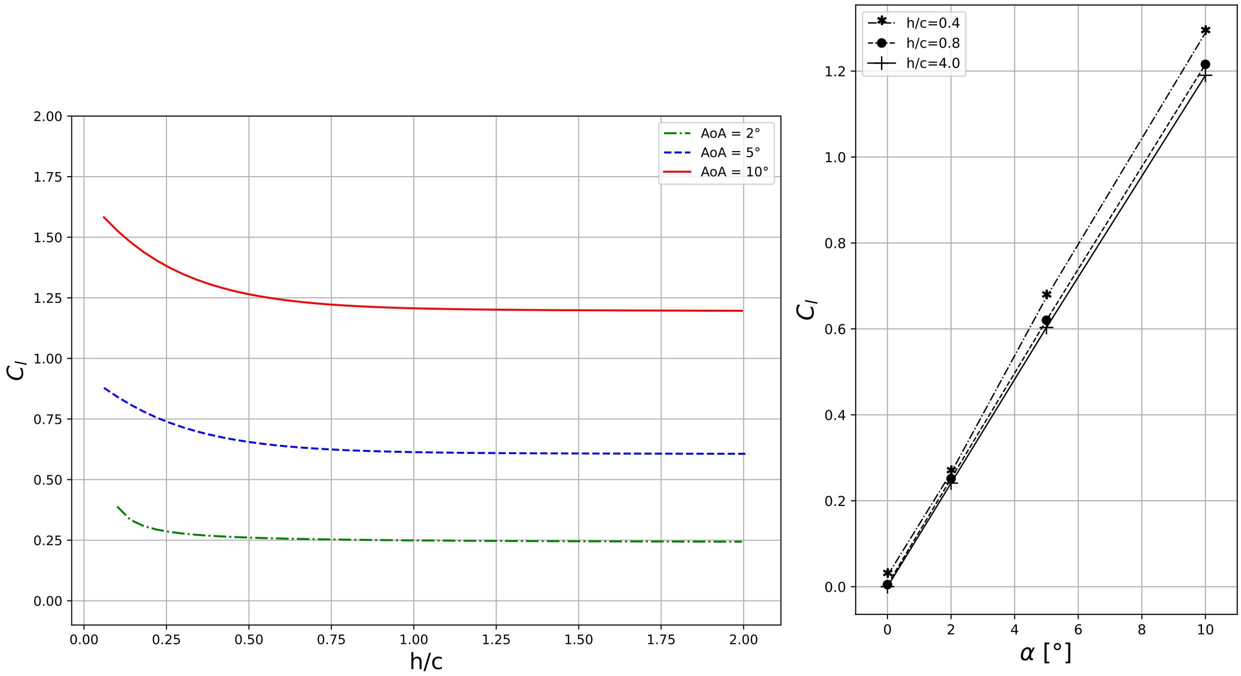

Figure 3.13: Lift coefficient from the mirror panel method as a function of h/c [left] and of AoA [right], 350 panels, NACA0012

(B.b) $F_h \to \infty$: Numerical solution to the "biplane image" problem

Similarly to what was done before, once the system for the "biplane" approximation (see Fig.3.14) has been solved, the circulation distribution $\gamma(s)$ and therefore the pressure coefficient distribution $C_p(s)$ are derived:

$$C_p(s) = \frac{p - p_\infty}{\rho\, U_\infty^2/2} \tag{3.15}$$

$$= 1 - (\frac{u_e(s)}{U_\infty})^2 = 1 - \frac{\gamma(s)^2}{U_\infty^2} \tag{3.16}$$

$$l = -\rho\, U_\infty\, \Gamma$$
$$C_l = \frac{-2\,\Gamma}{U_\infty\, c} \tag{3.17}$$

with $\Gamma = \int \gamma(x')\, dx'$

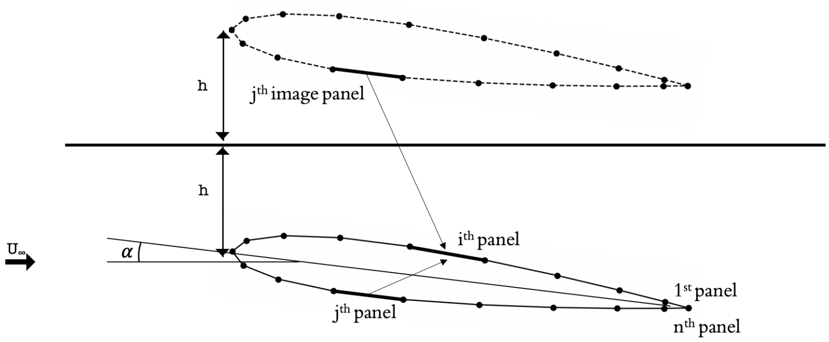

Figure 3.14: Biplane setup for panel code

On Fig. 3.15 is plotted the pressure coefficient $C_p(s)$ along the distance coordinate s measured along the airfoil, starting at the trailing edge and going clockwise. On this graph is shown the negative impact of a decrease of $\frac{h}{c}$ on the maximum negative pressure of the airfoil.

The lift coefficient obtained with Eq. 3.17 is plotted on Fig. 3.16 for an AoA = 5° for both the biplane *simplified model* and the *panel method*. The same conclusions as for the *mirror problem* are here again drawn, with a much more precise value for $\frac{h}{c} \to \infty$ and a non-infinite coefficient for $\frac{h}{c} \to 0$ for the panel resolution.

The impact of the AoA on the surface effect predicted by the "biplane" image panel method is shown on Fig.3.17. Looking at the left graph from right to left, the decrease rate of C_l with the surface approach seems constant with α, having up to 40% decrease in lift for the three AoA considered when reaching the minimal submergence depth.

Out of interest, the streamlines also obtained with the panel code are plotted on Fig. 3.18 for two different submergence depths.

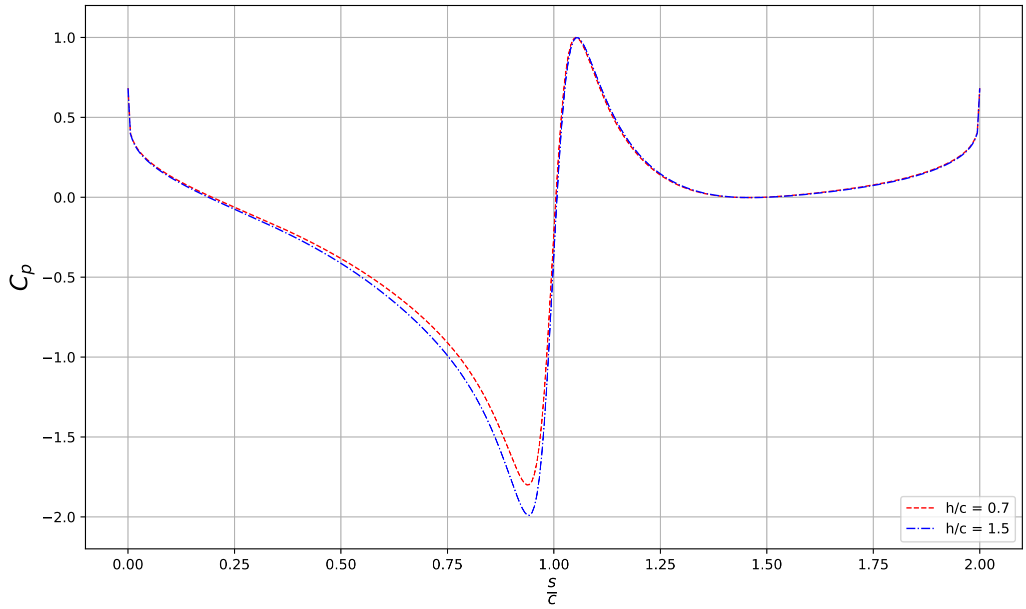

Figure 3.15: Pressure coefficients for different submergence depths, AoA=5°, NACA0012, 350panels

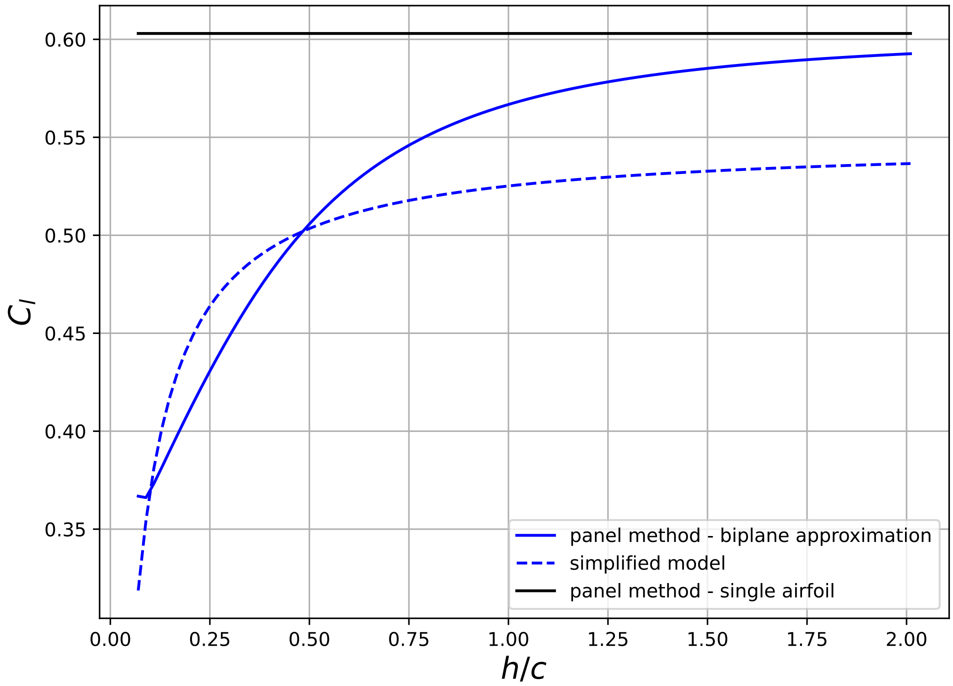

Figure 3.16: Lift coefficients as a function of submergence depth obtained by the different biplane models, AoA=5°, 250panels, NACA0012

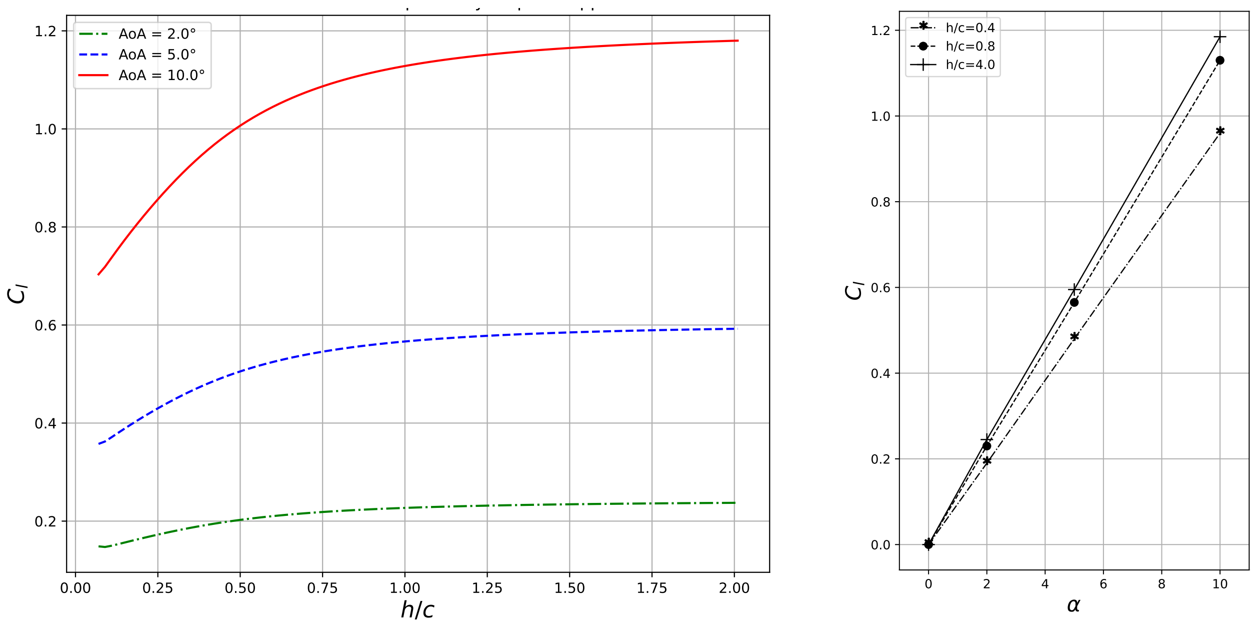

Figure 3.17: Lift coefficient from the biplane panel method as a function of h/c [left] and of AoA [right], 350 panels, NACA0012

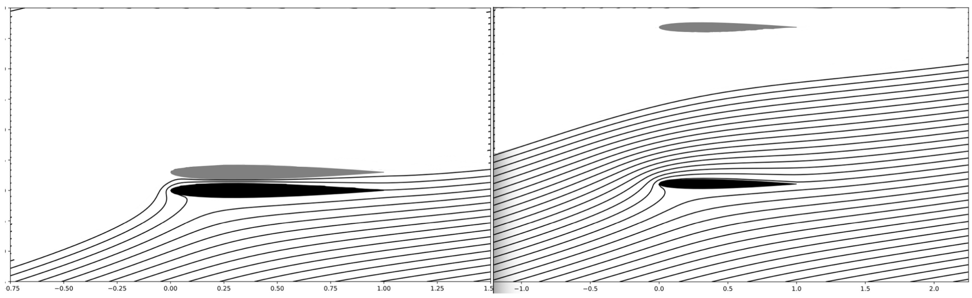

Figure 3.18: Biplane panel code streamlines calculation

Conclusions

In the case of the boat modelling considered in this work, the AC75 with foils of mean chord $\bar{c} = 0.4$ will start to lift-off at relatively low Fr_h but at such a high submergence depth that the free surface effects would be negligible. Then, as the hydrofoil gains lift by dynamic action, it follows that the Froude number will be high. These principal regimes of the boat are summarized in Table 3.5.

	$V_{boat}[m/s]$	$h_{tip}[m]$	h/c	F_h
Lift-off	≥ 7	2.75	6.875	≥ 1.35
Cruising (low ride-height)	18	1.4	3.5	4.9
Cruising (high ride-height)	18	0.05	0.125	25.7

Table 3.5

The low Froude number regime therefore mainly is of academic interest and will not be considered for the rest of this work.

Because of the potential flow calculations, it is important to remember that the model turns less accurate at very high Froude numbers when getting very close to the free surface because of risks of cavitation and ventilation. Those may cause a significant reduction in lift. As stated in [6], the lift coefficient of a supercavitating thin flat foil is $\frac{1}{2}\pi\,\alpha$, a quarter of its value without cavitation or ventilation.

3.3.2 C_L - 3D hydrofoil

The free surface effect will affect the 3D steady flow around a foil. The 2D effects developed in section 3.3.1 can be integrated in the lifting line theory to account for the free surface. The first part of the following section will investigate this approach while the next one will investigate a second one, consisting in the modelling of the 3D effects by adding a *biplane image 3D wing* above the surface in a similar way to what is done for wings in ground effect.

(A) Classical Lifting Line method

This first approach will, as introduced, solve a classic Prandtl Lifting Line method. In order to take the surface effect into account however, the 2D results will be integrated in Prandtl's compatibility equation by the means of the lift slope coefficient $a_0(y)$, computed with Section 3.3.1.

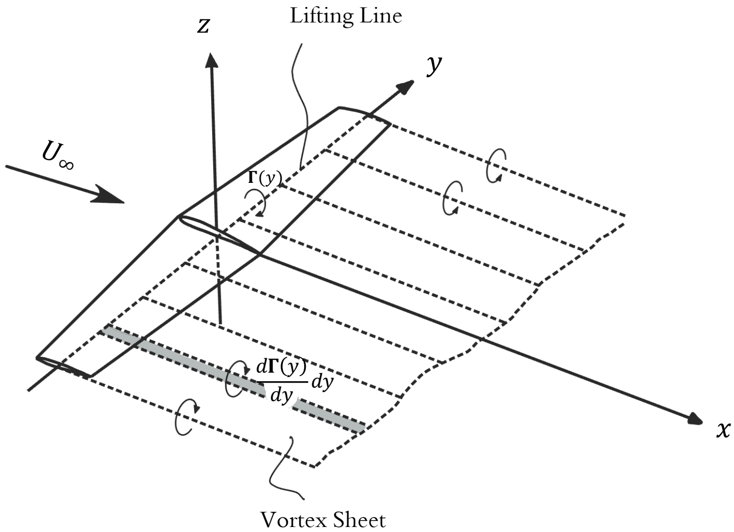

Figure 3.19: 3D wing - Classic Lifting Line configuration

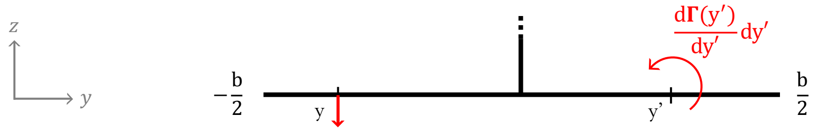

Figure 3.20: Classic PLL setup - downstream view

From Prandtl's compatibility equation with $a_0(y)$ being the lift slope coefficient of the profile located at y, computed with the *Biplane Panel Code* of Section 3.3.1:

$$\Gamma(y) = \frac{a_0(y)}{2}\, U_\infty\, c(y) \left[(\alpha - \alpha_0(y)) - \frac{w(y)}{U_\infty}\right] \tag{3.18}$$

with $\alpha_0 = 0$ if the profile has no camber and $\alpha(y) = \alpha$ if no twist is considered on the wing.

With the distribution of the downwash velocity $-w(y)$ that is obtained from the Biot-Savart velocity induced by the wake:

$$-w(y) = \frac{1}{4\pi}\int_{-b/2}^{b/2} [\frac{1}{y-y'}] \frac{d\Gamma(y')}{dy'}\, dy' \tag{3.19}$$

the downwash angle ϵ is then:

$$\epsilon = \frac{-w}{U_\infty} = -\frac{w(\theta)}{U_\infty} = \frac{1}{2\pi}\sum_n nB_n\ [\frac{\pi sin(n\theta)}{sin(\theta)}] \tag{3.20}$$

The system is subsequently solved with the following well-known change of variable and Fourier's series:

$$\begin{cases} y(\theta) = \frac{b}{2}cos(\theta) \qquad \text{with } 0 \leq \theta \leq \pi \\ \Gamma(\theta) = U_\infty b \sum_n B_n \cdot sin(n\theta) \\ \frac{d\Gamma(\theta)}{d\theta} = U_\infty b \sum_n nB_n \cdot cos(n\theta) \end{cases} \tag{3.21}$$

Solving the system in the sense of least squares for $N_{fourier} = 50$ and $N_{span} = 101$ will get the circulation distribution shown in Fig. 3.21 for a tapered wing with $c_{min} = 0.2[m]$, $c_{max} = 0.5[m]$ and a span $b = 4[m]$ for a $\delta_F = 0°$ and 30°.

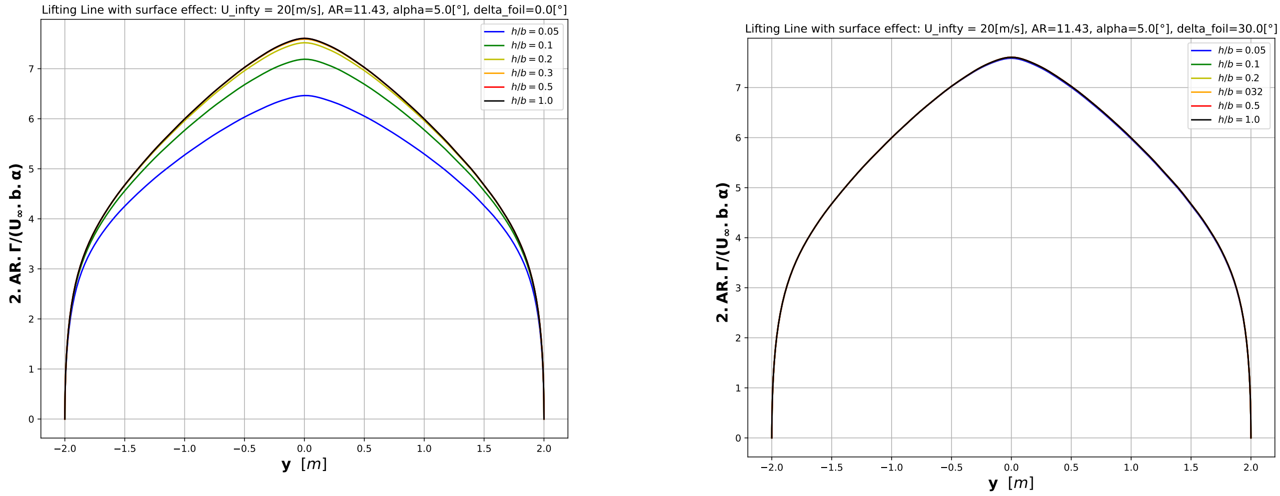

Figure 3.21: Classic PLL: circulation distribution with $\delta_F = 0^\circ$ and 30°

The lift and induced drag coefficients of the 3D foil are obtained as:

$$L = \frac{\rho\, U_\infty^2}{2}\, b^2\, \frac{\pi}{2} B_1 \qquad\qquad D_i = \frac{\rho\, U_\infty^2}{2} \frac{b^2}{2} \frac{\pi}{2} \sum_n n B_n^2$$

$$C_L = \frac{L}{\frac{\rho\, U_\infty^2}{2}\, S} = \frac{\pi}{2}\, A_R\, B_1 \qquad\qquad C_{D_i} = \frac{L}{\frac{\rho\, U_\infty^2}{2}\, S} = \frac{\pi}{4}\, A_R \sum_n n B_n^2 \tag{3.22}$$

Here after are plotted the results obtained for the lift coefficient and the induced drag coefficient as a function of the submergence ratio $\frac{h}{b}$ for different tilt angles of the foil. A 20% loss is observed for $\delta_F = 0^\circ$ when reaching a $\frac{h}{b} = 0.03$, which is in the case of the AC75's main foils a tip depth $h \approx 0.12[m]$. If the foil is tilted however, a fairly small impact of maximum 2% is predicted.

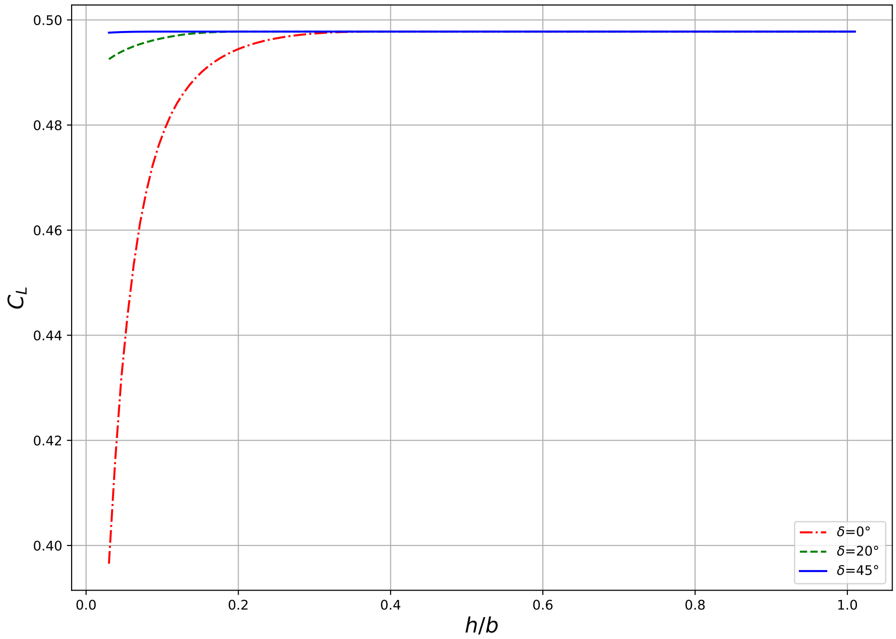

Figure 3.22: Classic PLL: lift coefficient as a function of submergence ratio for different tilt angles

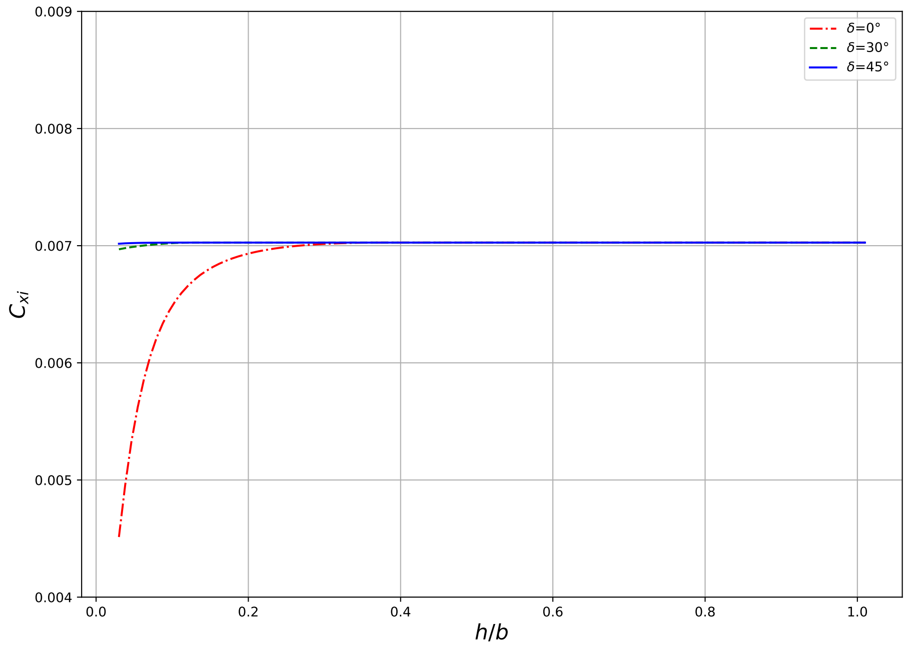

Figure 3.23: Classic PLL: induced drag coefficient as a function of submergence ratio for different tilt angles

(B) Biplane Lifting Line method

A standard approach to model the three-dimensional *wing in ground effect* is to add a mirror image vortex system underneath the ground. With the same reasoning as developed in introduction of section 3.3.1, the modelling of the three-dimensional *hydrofoil in free-surface effect* is done with the addition of a biplane image vortex system above the water surface. A schematic of this problem is provided on Fig.3.24.

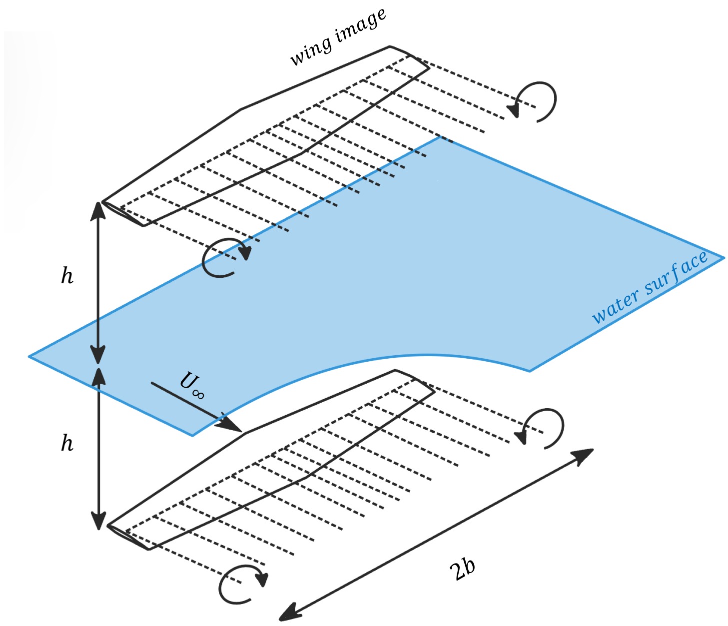

Figure 3.24: 3D wing - Biplane Lifting Line configuration

The specificity of the AC75's main foils is of course the fact that they do not operate parallel to the water surface but at an angle of tilt δ_F in order to produce anti-drift force. Such a lifting line is therefore more complex to model and solve. Fig.3.25 shows the downstream view of the problem, used for the developments below.

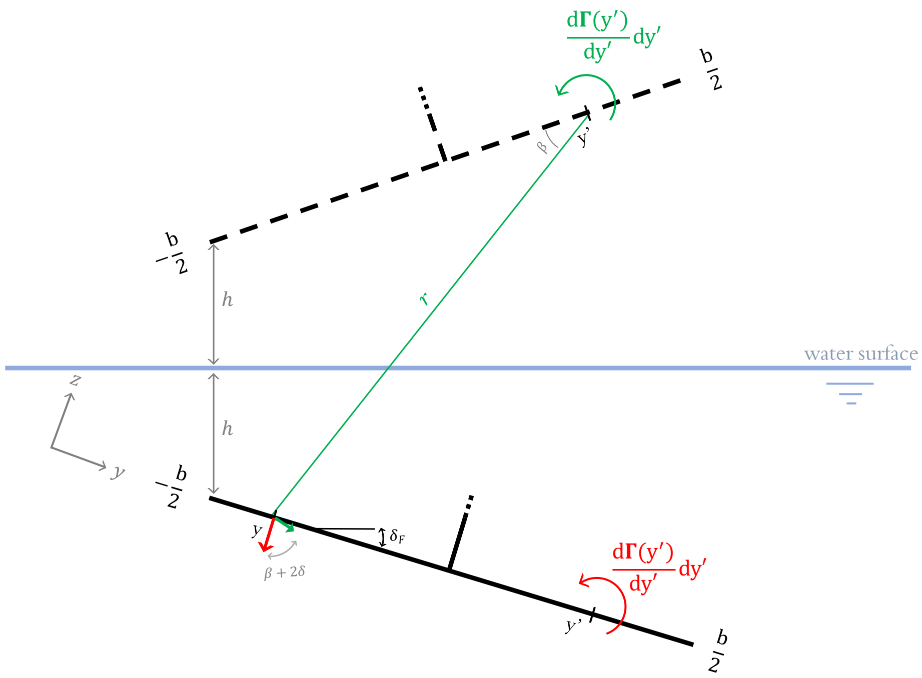

Figure 3.25: Biplane PLL setup - downstream view

The distribution of the downwash velocity $-w(y)$ is, again, obtained from the Biot-Savart velocity induced by the wake and, this time, *by its image* as well:

$$-w(y) = \frac{1}{4\pi}\int_{-b/2}^{b/2}[\frac{1}{y-y'} + \frac{cos(\beta+2\delta)}{r}]\frac{d\Gamma(y')}{dy'}\,dy' \tag{3.23}$$

with the same change of variable as the case without tilt, the downwash angle can be expressed as:

$$\epsilon(y) = -\frac{w(\theta)}{U_\infty} \tag{3.24}$$

$$= \frac{1}{2\pi}\sum_n nB_n\left[\frac{\pi sin(n\theta)}{sin(\theta)}\right. \tag{3.25}$$

$$\left. - \int_0^\pi \frac{(cos\theta - cos\theta')(cos\delta)^2 - (\frac{2h}{b/2} + (cos\theta + cos\theta')sin\delta)sin\delta}{(\frac{2h}{b/2} + (-2 - 3cos\theta + cos\theta')sin\delta)^2 + ((cos\theta - cos\theta')cos\delta)^2} \cdot cos(n\theta')\,d\theta'\right]$$

This integral will of course have to be numerically resolved before solving the system. More in-depth developments of the main calculation steps can be found in AppendixD.

Injecting this result in Prandtl compatibility equation (Eq.3.18) and solving the system in the sense of least squares for $N_{fourier} = 50$ and $N_{span} = 101$, we get the circulation distribution shown in Fig. 3.26 for a tapered wing with $c_{min} = 0.2[m]$, $c_{max} = 0.5[m]$, a span $b = 4[m]$ and a tilt angle $\delta = 0°$ and $30°$.

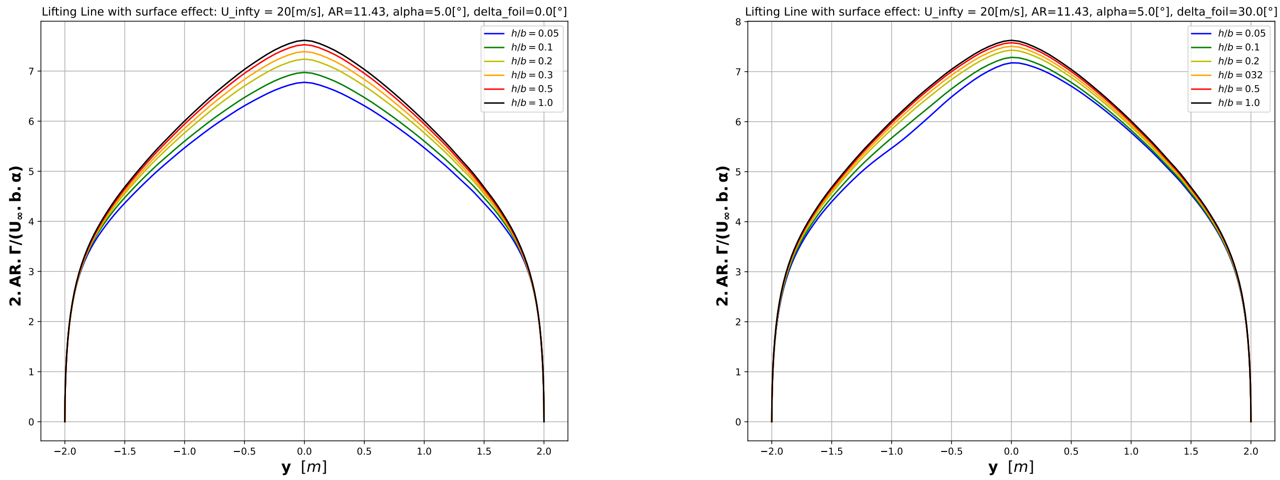

Figure 3.26: Biplane PLL: circulation distribution with $\delta_F = 0°$ and $30°$

The lift and induced drag coefficients obtained as a function of submergence depth are plotted on Fig.3.27 & 3.28. What can immediately be seen is a quite pronounced impact soon away from the water surface. With the wing tip approaching the surface, the loss in lift becomes more dramatic for the horizontal foil as well as the tilted ones. More in-depth discussions will be done when comparing the models just after.

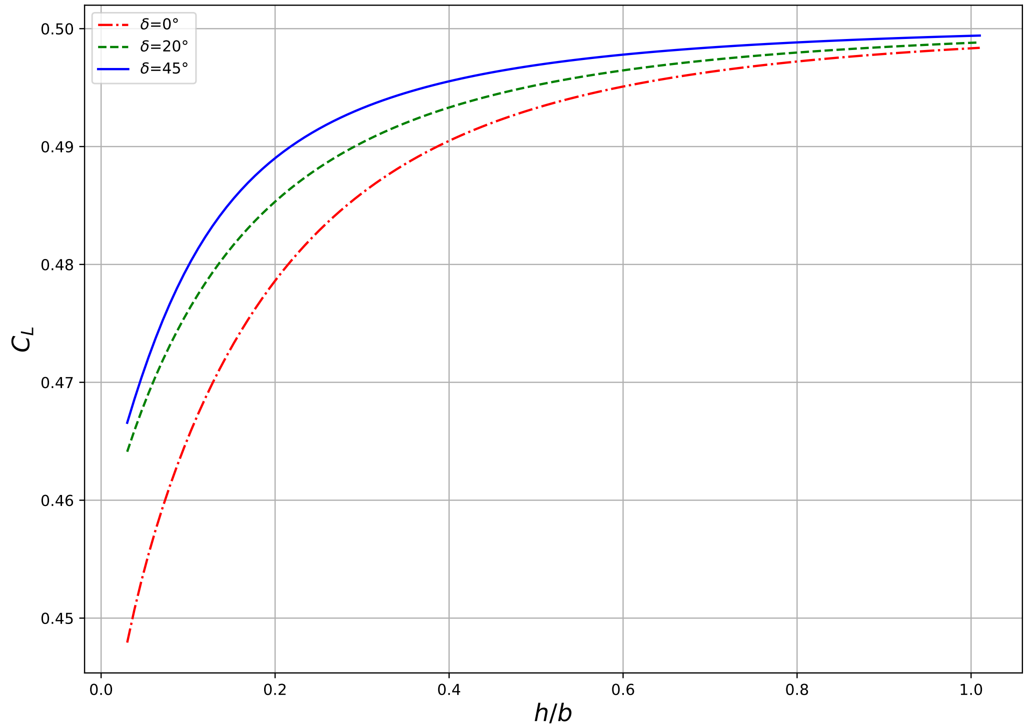

Figure 3.27: Biplane PLL: lift coefficient as a function of submergence ratio

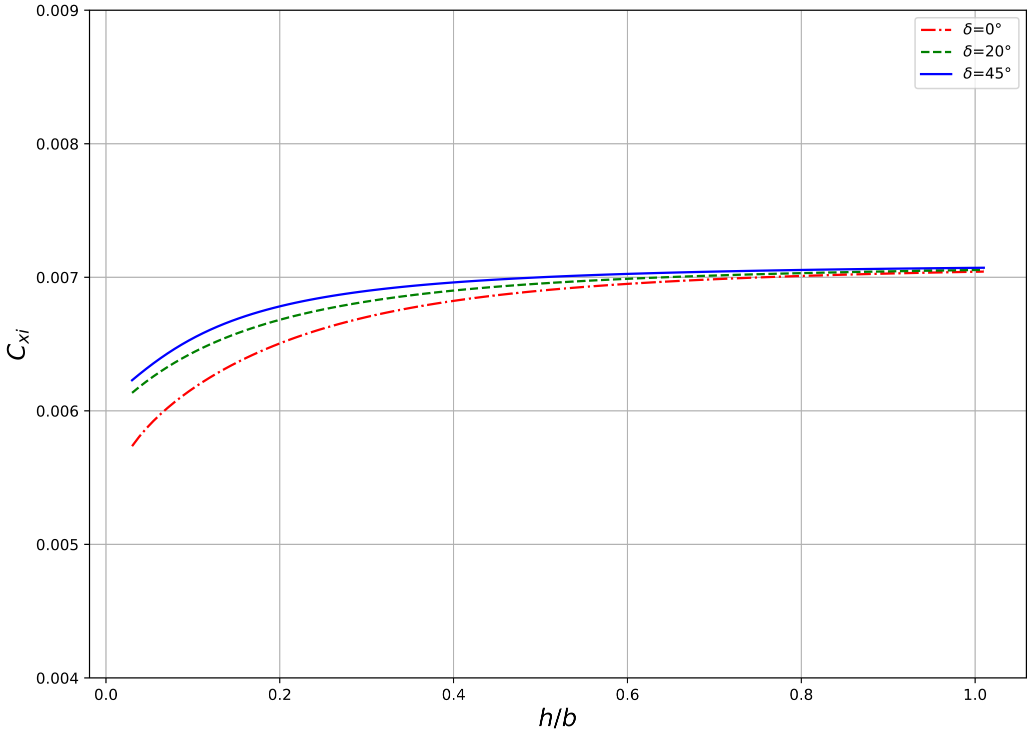

Figure 3.28: Biplane PLL: induced drag coefficient as a function of submergence ratio

(C) Comparison of the two approaches

A simplified model first written by DuCane, well known in the literature as the *'Simplified Biplane model'*, has been confronted with Wadlin *et al.*'s experimental data in Daskovsky's 1999 work [25]. DuCane adapted Glauert's unstaggered biplane theory to the case of the hydrofoil with the distance between the biplane foils being twice the submergence depth $2h$:

$$C_l = K \cdot a_0 \cdot \alpha$$

with $K = \frac{1+16\frac{h}{c}^2}{2+16\frac{h}{c}^2}$ obtained with a linearized boundary value problem represented as the sum of vortex distribution and source distribution [6].
To account for the 3D effects, the induced drag is increased by a factor of $(1+\sigma)$ where $\sigma = \frac{1}{1+12\frac{h}{b}}$ (curve fit). The 3D hydrofoil's lift coefficient is then:

$$C_L = \frac{a_0 \cdot K \cdot A_R}{A_R + 2K \cdot (1+\sigma)}$$

In Fig.3.29 is compared both Lifting Line approaches developed in this work to DuCane's model as well as Wadlin's experimental data. The sore point however is the fact that one can only compare lift coefficients for horizontal foils, that is $\delta_F = 0°$. Fig/3.29 shows that both models developed in this work converge towards the value of the wing without surface effect as soon as $\frac{h}{b} >\sim 0.8$. The 'classic PLL' model seems to acknowledge the presence of the free surface later than the 'Biplane PLL'. The 'Classic PLL' also seems to fit better the data for low values of $\frac{h}{b}$. This indeed makes sense, knowing that two-dimensional effects in $\frac{h}{c}$ will become of greater importance in a range [0,...,1.5], as shown on Fig.3.16.

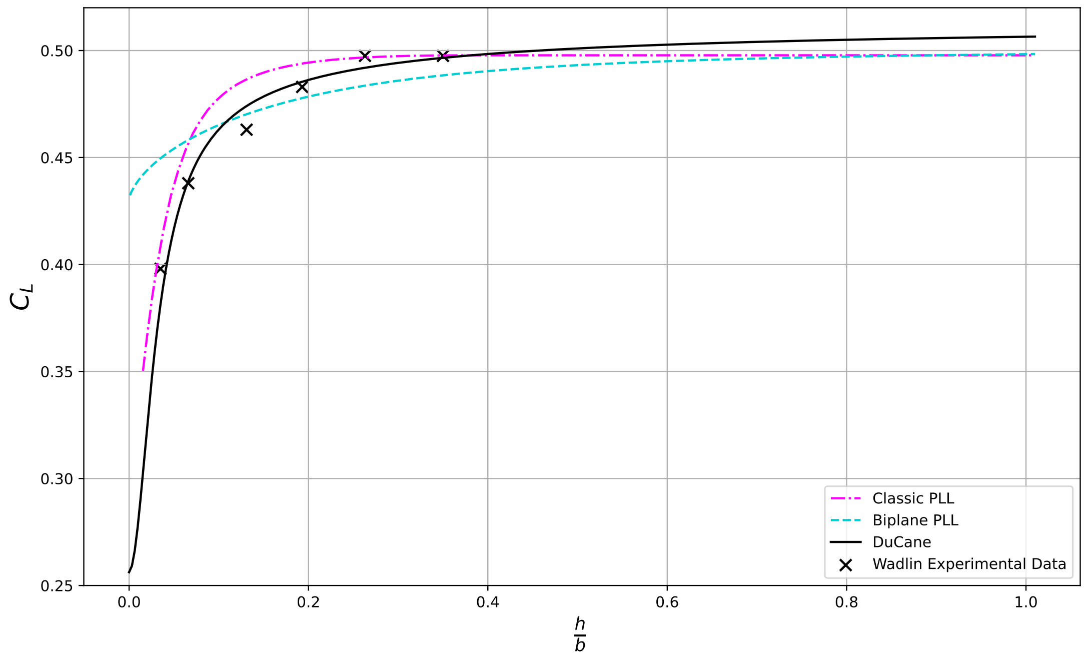

Figure 3.29: Lift coefficient comparison for the different models at $\alpha_F = 5°$, **with** $\boldsymbol{\delta_F = 0°}$

While it can be said that for $\delta_F = 0°$ and high values of $\frac{h}{b}$, the 'Biplane' Lifting Line follows the same behaviour as DuCane's formula, the 'Classic' Lifting Line seems to fit the data better for low values of $\frac{h}{b}$. What now remains to be found is whether this can be extended to the case of a tilted foil, that is $\boldsymbol{\delta_F \neq 0}$°.

An investigation of the downwash velocity distribution along the span $w(y)$ for both models, carried out at different submergence ratios and tilt angles, will show precisely where and how they both differ from one another. Before this, it is useful to remember that an elliptical planform wing will have a uniform downwash distribution along its span, whereas a tapered planform wing won't, as depicted on Fig.3.30.

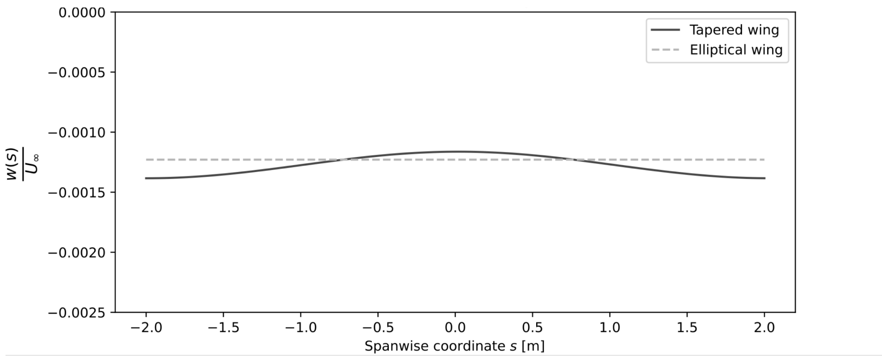

Figure 3.30: Downwash distribution for elliptical and tapered wings *out of surface effect*

The comparison of the downwash distributions is pictured on Fig.3.31 for both Lifting Line models at different submergence ratios $\frac{h}{b}$ and different tilt angles δ_F. Firstly, it can be observed that both models indeed tend to the same downwash distribution for high submergence ratios.

As mentioned back for Fig.3.22, the 'Classic' PLL doesn't see much of a surface effect as soon as the foil is tilted and keeps a very similar $w(y)$ for the range of submergence ratios considered. When $\delta_F = 0°$, it does manage to grasp an effect of the surface. This is obviously explained by the fact that the panel code implemented inside the Lifting Line takes account of the 2D influence that is known to be of importance for depth to *chord* ratios $\frac{h}{c} \in [0, .., 1]$, that is in this case $\frac{h}{b} \in [0, ..., \sim 0.0875]$.

The 'Biplane' PLL still sees an effect of the surface for way higher $\frac{h}{b}$ ratios, again as discussed for Fig.3.27. It can also be seen that a much larger asymmetric distribution is produced, being more negative towards the left tip, as it is the one closer to the water plane. For very low $\frac{h}{b}$, the 'Biplane' PLL produces a smaller downwash near the tips for a horizontal foil than for a tilted one, which seems quite counter-intuitive. As soon as the depth ratio becomes larger however, the right end that is well below the water surface gets more realistic downwash distributions. It is also interesting to note the dip in the distribution for low depth ratios observed at a quarter span from the shallow tip, which is believed to be mainly an exacerbation of the tapered wing intrinsic distribution, produced by the approach of the image Lifting Line above the surface.

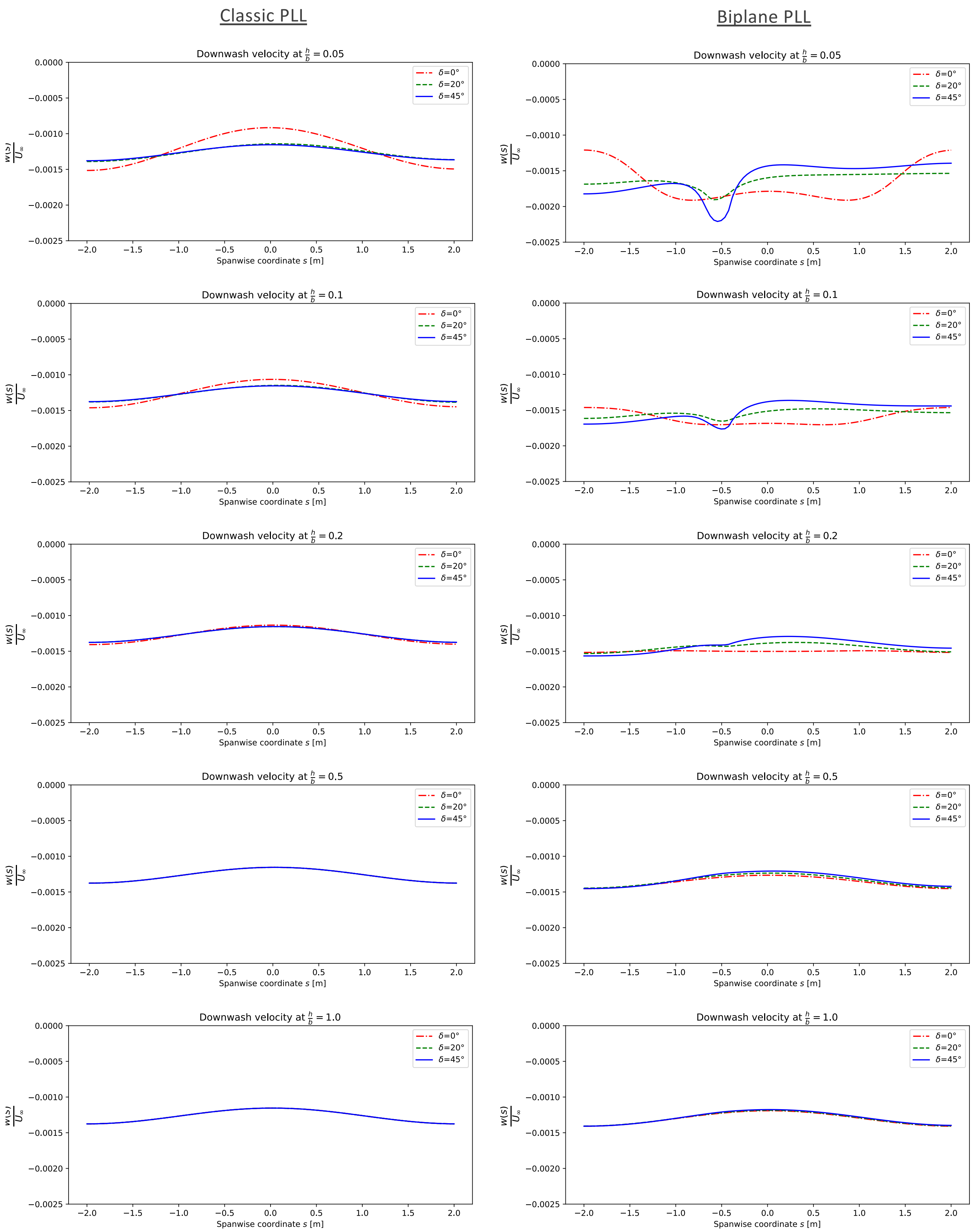

Figure 3.31: Downwash velocity distribution for different $\frac{h}{c}$ ratios: 'Classic' vs 'Biplane' PLL

Further adjustments:

Although an induced drag is modelled thanks to the lifting line, a profile drag remains to be evaluated. To do so, available data from XFoil[26] will be used in the model.

An implementation of stall is also added to the model by the means of a progressive decrease of the effective angle of attack, as from value around $\alpha_F = 12°$.

Because no flaps were developed in this model, it will be assumed for the further computations that flaps are not used when the boat is in regime, but are only used for the 'take-off' phase, which will not be studied.

3.4 Hull

The hull being exposed to high velocity airflow, a substantial drag results. The area exposed obviously depends on the apparent wind angle and was considered in the following simplified manner:

$$A_{hull} = \begin{cases} \text{AWA}\,\dfrac{A_{lat} - A_{front}}{90} + A_{front} & \text{if AWA} \leq 90° \\ (\text{AWA} - 90)\,\dfrac{A_{front} - A_{lat}}{90} + A_{lat} & \text{if AWA} > 90° \end{cases}$$

with the areas computed on the CAD model described in Section 3.1

The center of effort height is computed based on the ORC procedure [20] as follows:

$$Zce_{hull} = 0.66 \cdot \Big((0.625\, h_{front} + 0.375\, h_{rear}) + Bsin\theta\Big) \tag{3.26}$$

with B the boat's beam, h_front and h_rear being respectively the front and rear hull's projected heights, θ the heel angle.
A drag coefficient of 0.5 was used, a lower end value for highly profiled hulls [18].

3.5 Rudder

The rudder arm of the boat, requiring a no-camber profile in order to steer evenly, has been chosen with a NACA0012. Because of its very large span, no surface effects will be taken into account. The model will therefore use the panel code results for the 2D lift coefficient of a single profile in an infinite medium. Due to the presence of the rear foil under the rudder, effectively acting like a massive winglet device, an assumption of no induced drag will be considered here. Profile drag will be recovered from available XFoil predictions[26], as done for the main foils.

Stall will be handled by the means of a progressive reduction of the effective angle of attack, as done for the foils.

3.6 Implementation in Robotran

The multibody system of the boat will first be schematized on the *MBSysPad* graphical editor of Robotran. All six degrees of freedom of the boat will be implemented and each body will be defined by its mass, position of center of mass and inertia matrix. Each body is connected to one or a succession of parent *joint(s)*. A *joint* defines the relative motion between bodies. Fig.3.32 shows the boat model in *MBsysPad* with Robotran conventions as follows:

- $(\hat{I}_1, \hat{I}_2, \hat{I}_3) = (\hat{x}, \hat{y}, \hat{z})$ of Fig.2.1
- revolute and prismatic joints are denoted by the letters R & T
- joint positions are denoted by q, while velocities and forces by qd & Qq

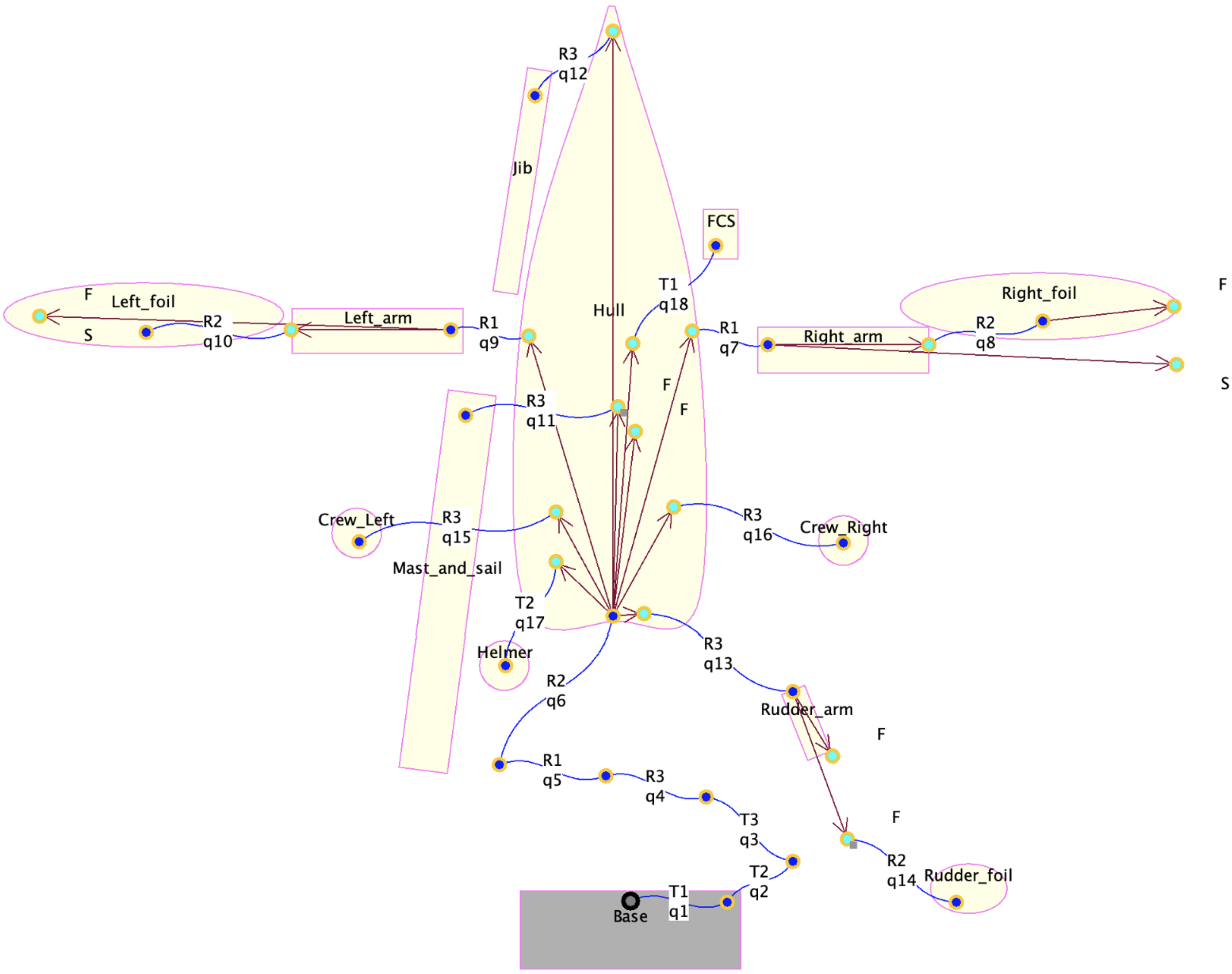

Figure 3.32: MBSysPad visualization of the AC75

On Fig.3.32 can also be seen *sensors*, denoted by 'S' and used to compute the kinematics of a point of the system. They will typically be useful for foil submergence depth measurements. *External forces* denoted by 'F' are used to impose a solicitation from the environment on to the system.

In MBSyspad is also entered a 'user model' containing the TWS and TWA values at which a configuration wants to be computed.

Once the *modeling phase* setting up the equations of motion that describe the multibody system for a given set of parameters and generalized coordinates is over, the *analysis phase* that uses the model to generate results such as equilibrium solution, modal analysis, time integration or optimization can be performed. From the MBSysPad configuration then, Robotran generates the multibody equations symbolically in the appropriate programming language. So-called symbolic multibody programs handle only arithmetical operators and strings of characters to produce the analytical form of the equations of motion, hence performing a time simulation way faster (with the same level of generality) than purely numerical ones where the model is rebuilt by numerous calls of subroutines every time a calculation is required [27].

Chapter 4

Velocity prediction

This chapter summarizes the major outcomes of this work. Through ROBOTRAN simulations, it will firstly try through a *two* degrees of freedom model to show the very undisclosed impact of some parameters that can be tuned in accordance with the AC75 regulations and, secondly, with *five* degree of freedom simulations, confirm the models and developments presented in the previous chapter.

4.1 ROBOTRAN velocity computation

The prediction of the velocities the boat is going to reach will result from equilibrium calculations and modal analyses made in ROBOTRAN. The two main input variables of this velocity prediction problem are directly linked to the wind itself: its speed and its angle of incidence, TWS and TWA. These two variables will dictate the propulsive force the sails can produce as well as the main resistance force, i.e. the hull's drag. As from a good enough initial guess of the independent variables q_u of the boat, the *'Equilibrium'* module will iterate to find the solution.

ROBOTRAN quasistatic equilibrium [28]

ROBOTRAN computes an equilibrium based on the reduced equations of motion where the generalized accelerations $\ddot{q_u}$ are set to zero. What remains is then the reduced force term as a set of non-linear equations:

$$F_r(q_u, \dot{q_u}) = 0 \tag{4.1}$$

This system will be numerically solved with the help of a Newton-Raphson scheme to get the equilibrium configuration.
The particular type of equilibrium of interest here is such that there is one (or more) joint i with a non-zero velocity $\dot{q_i}$. It is therefore said to be a quasistatic or dynamic equilibrium. Forces F_{qstc} act against resistance forces to maintain the boat in a continuous constant

motion. The computation of the steady-state equilibrium can be done in one of the following ways:

- Fixed speed $\dot{q}_i$ and x = $[q_u \backslash \{q_i\}, F_{qstc}]$
- Fixed force F_{qstc} and x = $[q_u \backslash \{q_i\}, \dot{q}_i]$

Here can be seen the notion of 'variable exchange', where the *joint position*, a non-sensitive variable, is replaced by a sensitive one being either the *quasistatic force* or the *joint velocity*.

In order to get the well-known *polar diagram* of the boat showing the best boat speed achieved across a range of wind angles, the equilibrium approach that was chosen was the latter, where by setting a TWS and a TWA, the external force (i.e. the force produced by the sails) was imposed. Robotran then iterates on the boat velocities and the other equilibrium variables up to convergence.

4.2 2 D.o.F. simulations - first stability intuitions

Two primary *two degrees of freedom* boat models were first studied by setting all the others to 'forced' zero values. Although not seeming particularly enthralling at first hand as to what is desired to be achieved, these simplified *dynamic equilibrium* calculations will allow a deep understanding of the boat's stability requirements. The main goal will here be to get a sense of the boat's velocity V_b such that the vertical equilibrium is achieved.

4.2.1 D.o.F. $= \boldsymbol{\phi}, \boldsymbol{\alpha_{rF}}$

During an equilibrium computation Robotran, will iterate on the independent variables $\boldsymbol{q_u}$ of the system, in this case the boat's pitch ϕ and the rudder foil's (a.k.a. rear foil) angle of attack α_{rF} (or $q6$ and $q14$ in Fig.3.32). However, one must check that the software chooses the correct variables but also the correct equations to be computed.

In Robotran's logic, a multibody system is composed of degrees of freedom, i.e. fictitious bodies before the boat's hull. A *forward kinematic* is executed in order to find the accelerations, then the forces are computed and a *backward dynamic* is executed. In the present case, it therefore means that setting the rudder foil's angle of attack and the hull's pitching as free variables would imply a computation of the equation on the *rudder*. While it would find its equilibrium, it will not help find the whole boat's equilibrium point.
A way around this will then be to use the notion of *variable exchange*, in order to focus on the correct dynamic equations while iterating on the variables of interest.

A first set of equilibrium calculations were therefore obtained by setting $T1_{hull}$ and $T3_{hull}$ as the free variables q_u of the system. The following variable exchanges were then executed:

- $q.T1_{hull} \longleftrightarrow q.R2_{hull}$: the boat longitudinal position, which is non-sensitive, is exchanged with the hull's pitch rotation

- $q.T3_{hull} \longleftrightarrow q.R2_{rudderFoil}$: the boat vertical position is forced to 0 by its exchange with the rudder's AoA

Because the vertical equilibrium equation was kept but the iteration was made on $q.R2_{rudderFoil}$, the iteration converges towards values for $q.R2_{hull}$ and $q.R2_{rudderFoil}$ so that $\sum F_z = 0$.

To produce these first quasistatic equilibriums, a boat velocity V_b therefore had to be fixed each time. These computations allowed for a better understanding of what range of speeds were going to be realistically achieved. Some examples are reproduced in Table 4.1 for a TWS=12kn and a TWA=50° .

V_b[m/s]	$R2_{hull}$[°]	$R2_{rudderFoil}$[°]	modal analysis (oscillating, unoscillating modes)
13.0	0.950	0.774	stable ($t_{1/2} = 13.8, 2310.5s$)
17.0	0.268	-1.593	stable ($t_{1/2} = 26.6, 14.8s$)
18.0	0.025	-1.480	stable ($t_{1/2} = 33.0, 12.72s$)
20.0	-0.491	-0.848	stable ($t_{1/2} = 64.18, 9.89s$)
25.0	no	convergence	/

Table 4.1: 2 D.o.F. ($\phi = R2_{hull}, \alpha_{rF} = R2_{rudderFoil}$ equilibrium results. TWS=12kn, TWA=50°

What can first be observed is that a too low V_b leads to a very lightly damped unoscillating mode and a too high V_b to a highly oscillating mode up even to no convergence reached for $V_b = 25.0$[m/s]. From first sight, the moderate velocities of around $17 - 18$[m/s] would give the best result, though still having a fairly high half-life $t_{1/2}$.

4.2.2 D.o.F. $= x, \phi$

The second 2 D.o.F. simulations executed concerned the surge velocity $\dot{x}$ and the pitch motion ϕ or $\dot{q}1$ and $q6$ on Fig.3.32. The following exchanges were executed:

- $q.T1_{hull} \longleftrightarrow q.R2_{hull}$: the boat longitudinal position, which is non-sensitive, is exchanged with the hull's pitch rotation

- $qd.T3_{hull} \longleftrightarrow qd.T1_{hull}$: the boat's vertical velocity is forced to 0 by its exchange with the boat's longitudinal velocity

Again, because the vertical equilibrium equation was kept but the iteration was made on $q.R2_{rudderFoil}$, the iteration converges towards values for $q.R2_{hull}$ and $q.R2_{rudderFoil}$ so that

$\sum F_z = 0$. If the hull's pitch had directly been set as a free variable, with for example $\boldsymbol{q_u}$ = $R2_{hull}, T2_{hull}$, and an exchange operated such as $qd.T2_{hull} \longleftrightarrow qd.T1_{hull}$, the lateral equilibrium equation would have been kept $\sum F_y = 0$.

In order to produce these first quasistatic equilibriums, a rudder foil angle of attack therefore had to be fixed each time. With a possible future dynamic control in mind, each configuration will be chosen with two constraints on the rear foil angle of attack:

- it can be adjusted with a half degree precision:

$$\alpha_{rF} \in \pm\Big[0, 0.5, 1, ..., 8\Big]^{\circ}$$

- it is close to the AoA from the neighbouring configurations of the boat:

$$\alpha_{rF}(\text{TWS,TWA}) \in \Big[\alpha_{rF}(\text{TWS,TWA}_{-1}), \alpha_{rF}(\text{TWS,TWA}_{+1})\Big]$$

4.2.3 Modal analyses with D.o.F. = $\dot{x}, \phi$

Throughout the following parametric study, various modal analyses will be carried out to study the influence of these parameters on the boat's stability. It can be a powerful tool to adjust a design up to an expected behaviour as has been shown by A. Bagué for a viper foiling boat [29]. The following ananlyses will be based on a similar methodology. Some details about modal analyses can be found in the Robotran documentation [28] and additional information is provided in Dr. Rheinboldt's notes [30].

First and foremost, it is important to specify that, during a modal analysis, the independent variables $T1_{hull}$ and $T3_{hull}$ that were frozen during the equilibrium module are unfrozen here. The boat thus has two independent variables which lead to four eigenmodes. As mentioned before, the longitudinal position of the boat does not impact the general equilibrium of the boat in any way whatsoever, as explained in Drela's book on flight vehicle aerodynamics [31]. The eigenvalue associated to this mode, the first mode, is therefore null. The eigenvector of the mode is the null space vector $[1 \;\; 0 \;\; 0 \;\; 0]^T$. It will not be further discussed as it is not relevant for what follows.
The second eigenvalue is the complex conjugate of the third. This indicates that they form one joint eigenmode. They correspond to small perturbations in the vertical direction $T3_{hull}$ of the boat. Its oscillatory behaviour comes from the fact that, when rising and approaching the free surface, the main foil loses lift. The draft of the ship then decreases and the foil regain lift. The mode makes the boat slowly oscillate towards stable equilibrium. This oscillatory behaviour has a very low frequency and also a very low damping conduct as will be seen further.
The fourth mode is seen to always be non-oscillating unstable for the configuration studied in this 2 D.o.F model. It corresponds to a small perturbation on longitudinal speed. This result shows that the AC75 does not easily have a global dynamic stability and needs active

control at all times. Indeed, a subtle change in wind direction or wind speed results in a change in equilibrium speed, which directly impacts the sails outputs and the foil outputs squared simultaneously. This can snowball into the loss of foiling equilibrium and a shift to displacement regime with the hull in the water. Modes 2,3 and 4 will be discussed in details during the parametric study.

4.2.4 Varying the dimensions of the boat's main elements

This section aims at giving a better insight into the phenomena that occur when some changes are made on certain design dimensions or positions of parts of the boat. Specific attention will be given to how the varying parameter influences the general equilibrium speed of the boat, how it affects its general stability and what is the explanation behind it all. The reference TWS is set to 7.2 kn and the TWA to 151.5°. Throughout the chapter, the positions will be expressed in relation to three reference planes. The first, the MWP (Measurement Waterline Plane), is the horizontal plane located at the bottom of the hull. A clear image of it can be seen in Fig.3.1. The second reference plane is the LCP (Longitudinal Center Plane) and is cutting the boat in a left and right half. Considering the rather symmetrical design of the boat, it will be seldom used. The last reference plane, the TRP (Transom Reference Plane), is located entirely aft (at the back) of the boat with its normal oriented in the longitudinal direction of the boat. The three planes are, of course, perpendicular to each other.

Main foil span

The main foil span plays a crucial part in the mechanics of the sailboat. The design of an AC75 relies entirely on trade-offs. Foils with high top speeds will not have high manoeuvring speeds and this might need to be compensated by adjusting other parameters. Foils with high top speeds are typically short foils [32]. Short foils have the advantage to generate less drag at a fixed course direction in foiling mode and thus have a higher top speed as can be seen on Fig.4.1. It also shows the clear correlation between top speed and drag reduction. The lift will be lessened for shorter spanned foils that still produce the required lift. However, during specific manoeuvres such as tacking, the speeds at which the crew performs the manoeuver might be too low for the sailboat to maintain its foiling mode. At that moment the boat might go back to the most stable regime of them all, i.e. with the hull back in the water. The team will then lose some precious time trying to go back to foiling mode after the manoeuvring. Bigger spans have also the advantage to ensure a quicker foiling response time: they can get the boat up and foiling earlier than smaller spanned foils. All these play a key role in the design philosophy of the boat.

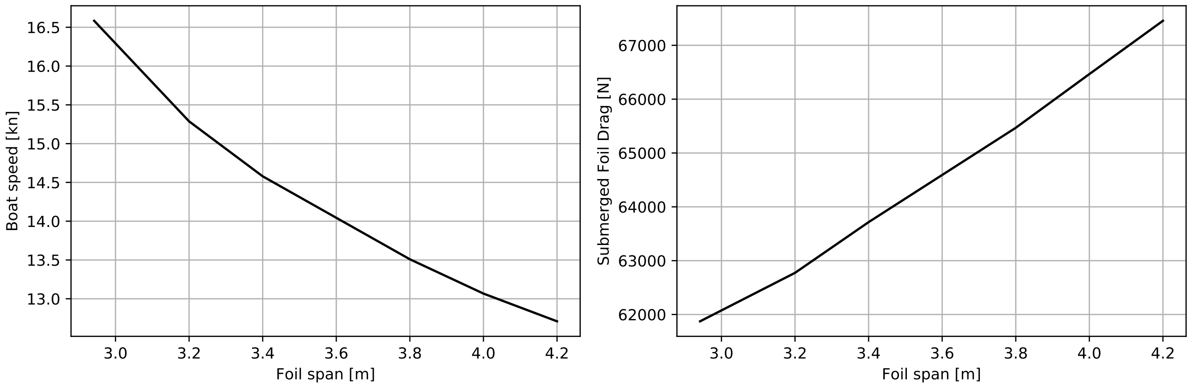

Figure 4.1: Top speed and drag variation as a function of main foil span

Concerning the modal parametric analysis, some interesting observations can be made. It is interesting to note that modes 2 and 3 form a complex conjugate pair for every value of span of 3.4m and less. When the span reaches a threshold, located between 3.4 and 3.8m, the eigenvalues become purely real and make place to two distinct modes. This means that, because they reach the surface quicker, the lift loss will instantly "drop" the boat back to a conventional depth without oscillations. This seems fairly logical given that foils with larger spans exert more lift in the same equilibrium conditions. Mode 2 becomes non-oscillatory stable and its stabilizing behaviour increases with the span expansion. Mode 3 emerges and becomes non-oscillatory unstable with an increase in instability linked to a span expansion. To conclude, on a racing point of view, the span of the foil should be determined based on the general philosophy of the ship: is a high top speed, low transition time to foiling, high manoeuvrability etc. desired? Stability wise, shorter foils do not make the boat significantly more stable but they reduce very slightly the rate at which the boat becomes unstable in mode 4. Focus should then be put on the racing capacity of the boat rather than improving its stability by varying the main foil span.

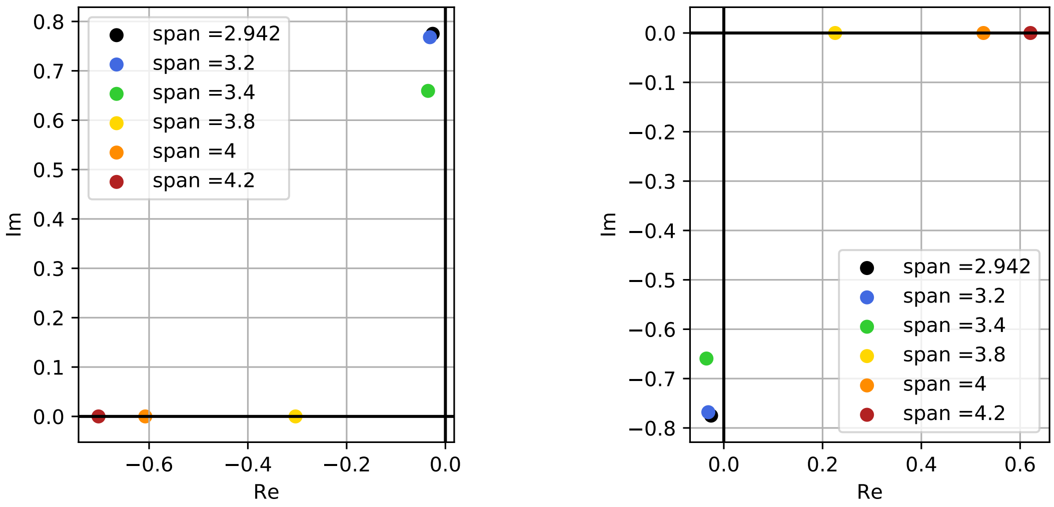

Figure 4.2: Modes 2 and 3 of quasi-static equilibrium with varying main foil span

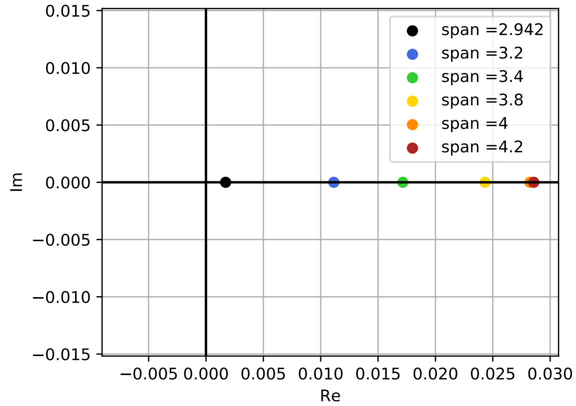

Figure 4.3: Modes 4 of quasi-static equilibrium with varying main foil span

Rudder advance

Another parameter which the teams can act upon is the advance of the rudder, upon which the rear foil is attached, with respect to the TRP. The entirety of the rudder must lie between the TRP and a plane 1.5m in front of and parallel to it. In reality, the control on the rear foil is made by changing its rake. This is done by rotating the rudder transversely about its attachment point to the hull. However this has not been modelled exactly the same way in ROBOTRAN. Indeed, the control of the rear foil AoA has been implemented with a transverse rotation at the end of the rudder. On a design point of view, the rudder has to be placed as far away aft of the boat as possible. This bears two reasons: first, the rear foil has to be as far away as possible of the disturbed wake of the main foils to have an optimal working environment and secondly, the role of the rudder is to control the yaw of the boat and advancing it will reduce its lever arm and ultimately its manoeuvrability, as explained by J. Sans [33]. It must be borne in mind that, needing to change its rake to control the rear foil, it may not be placed completely at the end of the boat. In that case the rear foil might exceed the limit of the TRP in an attempt of the team to rake it positively. In a similar way, it should not be placed too far forward of the TRP. Advancing the rudder has a negligible impact on top speed. Physically there should be a top speed decrease due to the foils wake, this can thus be considered as one of the limitations of the model.

The modal analyses reveal that none of the four modes vary with the rudder advance, their values remain exactly the same no matter what. The second and third modes are complex conjugates that indicate an oscillatory damped behaviour. The fourth mode remains non-oscillatory unstable. A theoretical conclusion is that the rudder should be placed as far back as possible with some spare space to change the rudder's rake. However it is rather intriguing to notice that the rudder's advance, which is a key parameter in the pitching of the ship, does not play that big of a role in the general equilibrium of the ship.

Main Foil Arm Position

The position of the arm to which the main foil is attached may vary from 9.95m to 12m in front of the TRP. The effect of advancing the main foil arm has mainly an impact on the lever arm of the foil. An increased foil lever arm will unload the foil a little bit and will load the rear foil more. This is why the main foils lift diminishes with the foil arm advance, while the rear foil lift increases as can be seen in Fig.4.4. Given that the main foil has a broader span than the rear foil, unloading the main foil makes for a marginal foil drag reduction. This is reflected with an almost negligible rise in the top speed of the boat. On a racing point of view, it is slightly more beneficial to advance the main foil to the most.

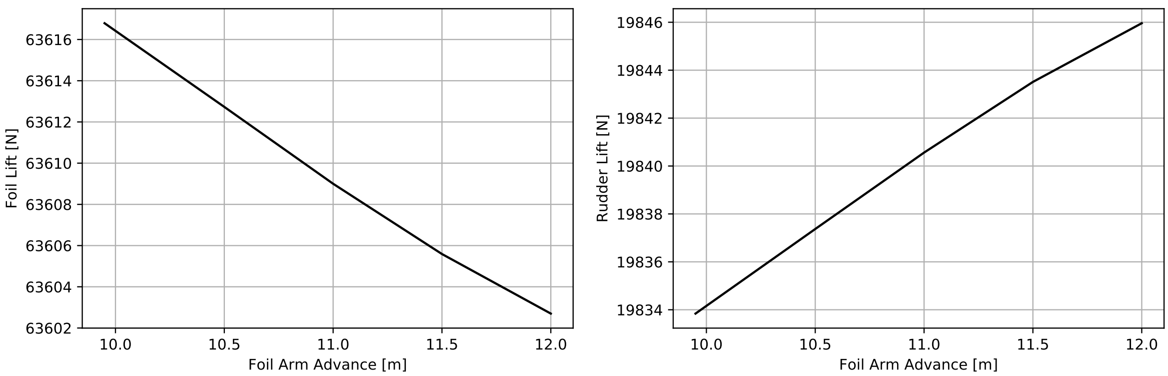

Figure 4.4: Lift of submerged foil and rear as a function of main foil arm advance w.r.t. TRP

Stability wise it does not entirely tell the same story. The second mode and the third mode are again complex conjugates. All the eigenvalues are located at roughly the same real part, which means that this mode does not gain any stability by varying the foil arm position. The half life of this mode $t_{\frac{1}{2}} = \frac{ln(2)}{\lambda}$ is 28.5s for an advance of 10.5m. This means that it will lose 50% of its amplitude after that amount of time. This is a very low response time and its consequences could ripple through and impact the control of the boat over long periods of time. Only the eigenfrequency will be different and its distribution seems to be very binary. The eigenvector of that mode has been plotted in figure 4.5 to analyse what variable influences it the most. The blue arrow symbolises $\Delta \dot{T1}_{hull}$, the small speed variation. The black arrow symbolises $\Delta T3_{hull}$, the small height variation. It is interesting to note that those are almost perfectly out of phase. When the boat speeds up it will rise, when approaching too close to the surface it will slow down which will in turn lower the boat. The green and red arrows symbolise respectively the pitch $R2_{hull}$ and advance $T1_{hull}$ of the boat. The fourth mode does not vary linearly with the main foil arm advance. As can be seen on figure 4.6, there is a minimum value obtained for an advance of 11m. Given the negligible gain in top speed, a focus should be placed on getting a less unstable boat, even though that gain is also extremely low.

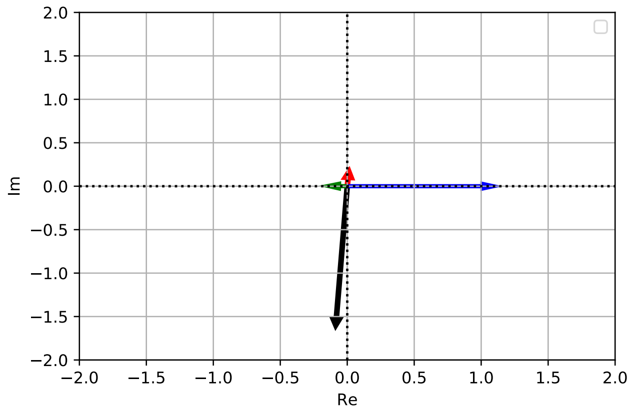

Figure 4.5: Eigenvector of second mode with foil arm position at 10.5m w.r.t. TRP

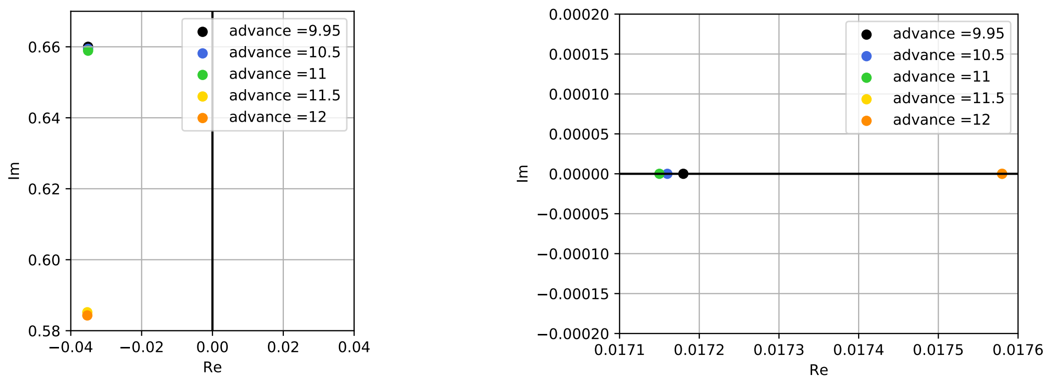

Figure 4.6: Mode 2 and mode 4 w.r.t. main foil arm advance

Rudder Depth

The Rudder has a maximum allowed depth of 3.5m below the MWP. During the analyses, the maximum displayed depth can reach 3.9m, this depth is still in accordance with the rules because it is measured from the top of the hull. It is thus tens of centimeters higher than the limits expressed by the class rules. Deepening the rudder has a negative impact on the boat's top speed. It has the effect to distribute the load more evenly between the main foil and the rear foil. The main foil has a strong anti drift function whereas the rear foil has a solely stabilising role by raising the aft of the boat and creating two control points on the foiling mode of the boat. Deepening the rear foil means a marginal change in equilibrium pitch of the sailboat whereas it could mean a strong anti drift loss. In this case, the anti drift loss is not felt by the model because $T2_{hull}$ has been "locked" but in reality it could be a very likely outcome. The load redistribution will pitch the boat slightly backwards. This pitch variation comes with an increase of the AoA of both foils and thus a higher drag. This results in a top speed decrease as can be seen in Fig.4.7. Let's note that an infinitesimal change in pitch translates into a slightly bigger change in top speed which puts forward how sensitive the general equilibrium is.

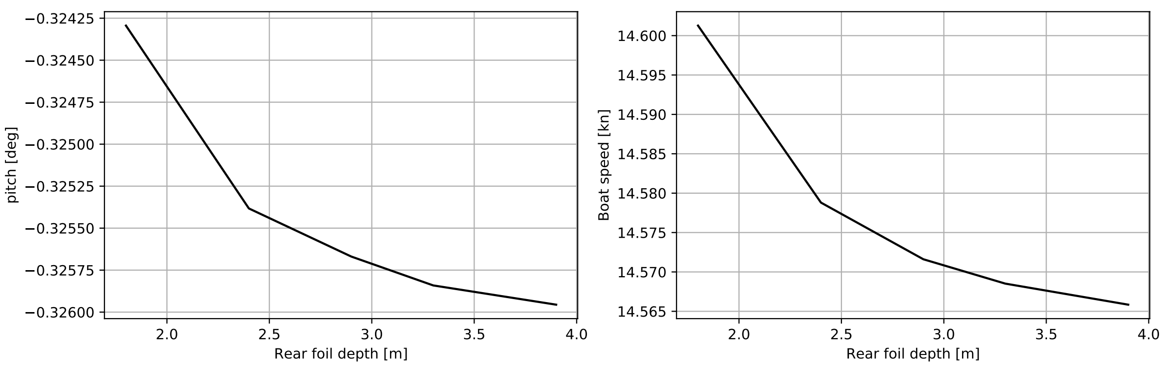

Figure 4.7: Pitch and boat speed as a function of rear foil depth

The modal analysis, again, gives a conjugate complex second and third mode. The depth of the rear foil does not change the stabilising behaviour of the boat, however it changes the frequency of the mode. A deeper rear foil will have a smaller oscillating frequency. Indeed, a bigger pitch inducing a bigger AoA will also induce a lift gain. The boat will approach the free surface quicker and will thus have a higher eigenfrequency. Concerning the fourth mode, a deeper rear foil means a more positive eigenvalue (see Fig.4.8) and thus going to instability "quicker". The theoretical conclusion might be to design the rear foil as shallow as possible. Bear in mind that, in the reality, a shallower rear foil means that the equilibrium height of the aft of the boat is also closer to the water level and thus more prone to being disturbed by waves and disrupting the general stability of the sailboat. It is always important to confront the model to the reality. Again, a trade off has to be found in accordance with all the other parameters.

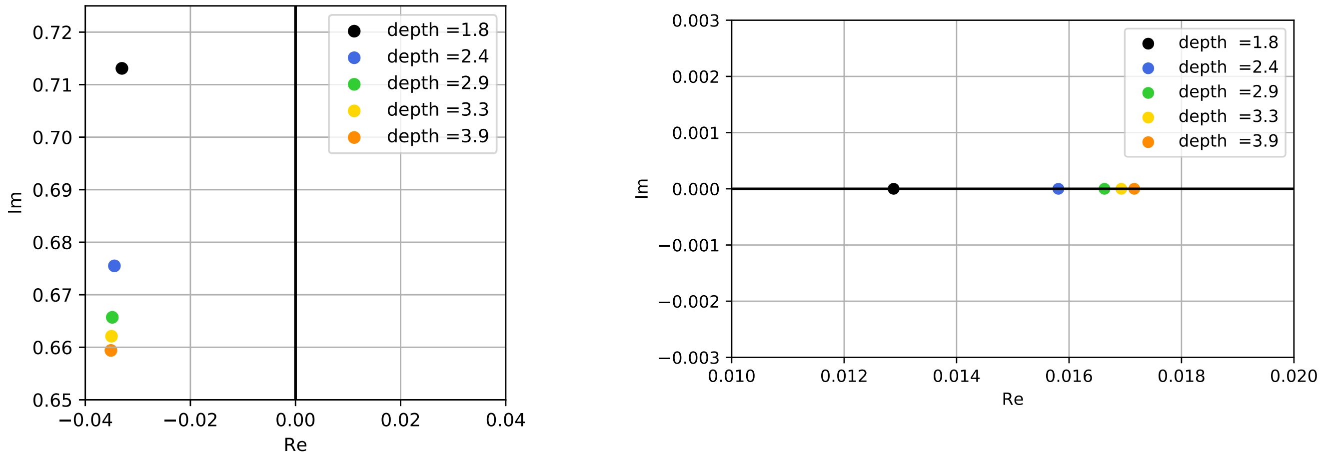

Figure 4.8: Second and fourth mode in function of rear foil depth

Foil span with different TWS

The same parametric study as before will be conducted, this time the TWS is not 7.2 kn but 10.1 kn. This slightly reduces the AWA and increases AWS as the TWS gains more "weight". The objective is to see if the conclusion drawn in the previous paragraphs are independent of the point of sail or not.

The case of varying foil span is presented because it was the most impacting previously. As before, the top speed decreases when the main foil span increases. Again, this is due to a drag increase directly linked to a wider span. The modal analyses reveal a similar pattern as before (see figure 4.9). One thing to notice is that, with those initial conditions and a TWS that gets more weight in the AWS it reduces the equilibrium speed of the boat. Smaller foils do not have the capacity to converge to an equilibrium with those initial conditions, the configuration does not provide enough lift. Two conclusions can be drawn: First, the modes of the sailboat do not rely on the point of sail. The eigenvalues of the modes might change in magnitude but negative real values will remain negative. This is because even though true wind has a clear impact on the equilibrium, the dynamic wind still prevails as long as the true wind ranges in reasonable values. In storm conditions, the boat becomes, obviously, too hard to stabilise in foiling mode. Other parameter variations show similar modal results as here and were not presented for the sake of soberness. Secondly, the conclusions drawn for one point of sail concerning the effects of the parameters on the top speed or time to foiling or tacking stability might not be applicable for other points of sail. The eigenmodes remain the same but the effects on top speed etc. not necessarily.

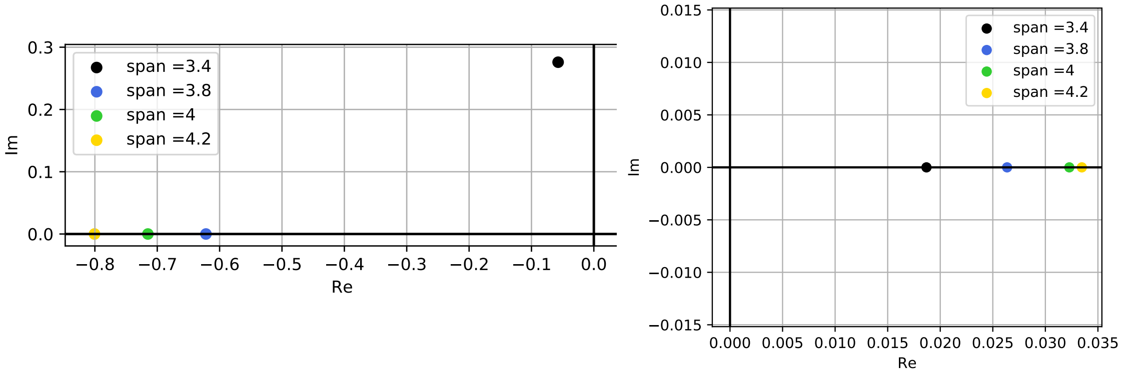

Figure 4.9: Second and fourth mode as a function of foil span with TWS = 10.1 kn

Foil span with different TWA

Now that it has been asserted that the modes do not drastically change of behaviour when subject to a varying TWS, let's analyse how the boat behaves with a varying TWA. The TWS remains 10.1 kn and the TWA goes from 151.1 to 120.3 deg.

Again, the foil span will be the varying parameter given its high impact on the general equilibrium. An observation can be made on the second and third mode: there no longer is an oscillating behavior as they are both always real. A shorter span has a less stabilising behaviour than a longer span as it was the case for the previous TWA of 151.1 degrees. This shows that the TWA variation does not impact drastically the eigenmodes of the sailboat. Let's note that the second mode here has a bigger stabilising effect than observed before. Its half life is now in the order of 0.7s which highly strengthens its stability. The lower TWA removes the boat further away from the peak VMG as will be explained later on. The TWA seems to have a certain impact on boat speed that, in turn, has a huge impact on the boat's stability.

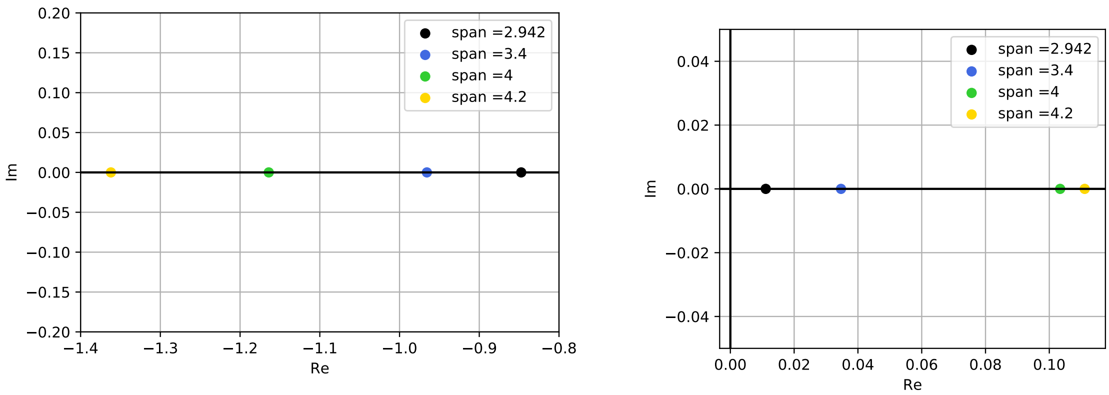

Figure 4.10: Second and fourth mode as a function of foil span with TWA = 120.3 deg

Conclusion

To conclude, the adjustments of all the boat parameters have a globally small influence on equilibrium speed and stability. Still there has to be coherence between all the choices that the teams have to make to benefit from the best trade-off between stability and speed. Being a high performance sport, every small design choice could result in an overall huge advantage over the other teams. Concerning the 2 DoF model, it gives an insight on the stability behaviour of the ship and clearly marks that active control has to be set up to keep the boat in foiling mode. This is done in real life by continuously changing sail trim, foil cant and rear foil rake. These actions are combined with a clear monitoring of the wind and the boat parameters through various sensors. All the modes studied in this chapter have a very high half life and that half life greatly decreases when the boat navigates at lower speeds. The negative impact of boat speed variation has been put forward several times in the chapter through the fourth mode.

4.3 5 D.o.F. simulations - validation of the model

In this section, a *five degrees of freedom* model is used for the simulations. Those five degrees will be $(\boldsymbol{x}, \boldsymbol{y}, \boldsymbol{z}, \boldsymbol{\theta}, \boldsymbol{\phi})$ respectively the surge, the sway, the heave, the heel and the pitch motions of the boat. Because of not much interest for optimal velocities computation, the yaw motion of the boat has been omitted in order to limit the number of equations to resolve and ease the convergence. With the same reasoning as previously explained in Sections 4.2.1 & 4.2.2, variable exchanges are performed:

- $q.T1_{hull} \longleftrightarrow q.R2_{rudderFoil}$: the boat longitudinal position which is non-sensitive is exchanged with the rear foil's pitch rotation in other words its angle of attack.

- $qd.R3_{hull} \longleftrightarrow qd.T1hull$: the boat's angular velocity around the *z-axis* is fixed to 0 by its exchange with the hull's longitudinal velocity.

Due to the very competitive nature of the discipline, very little data from the 36th America's Cup races is available for checking how the model fits the reality. Nevertheless, some fundamental figures can be found and will be used in the following section. For instance, Fig.4.11 depicts the True Wind Speed experienced by *Emirates Team New Zealand*'s boat during the first race of the 36th America's Cup. It can be seen that this wind velocity is mainly within a range of values $\sim [12.0, ..., 14.0]kn$ = $[22.2...25.9]km/h$. This range, being representative of the middle to upper values encountered across all the races of the 36th America's Cup as well as being a range where no reefing of the sails is needed, will be the one considered for the validation of the model.

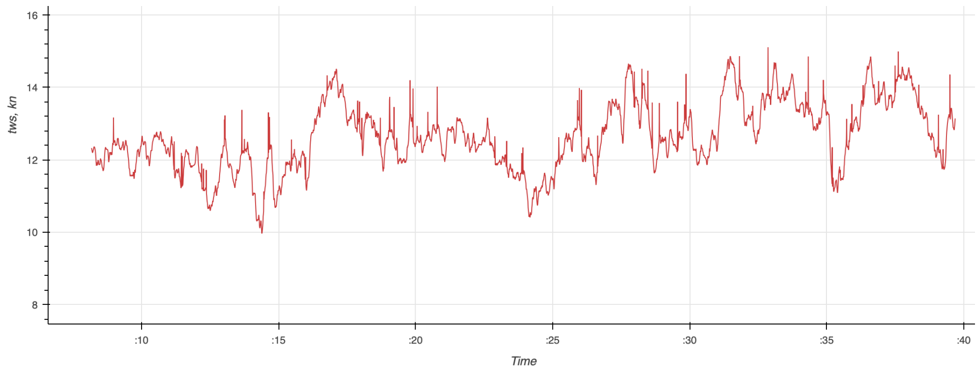

Figure 4.11: TWS - Race data [7]

4.3.1 Boat velocity prediction

The velocity prediction results presented hereafter use the NACA-0012 foil profile with an angle of attack $\alpha_F = 2.5[°]$. Different angles of attack were analyzed in the model, with $2.5[°]$ offering the best overall boat velocity across a range of TWS but also the largest number of *stable* equilibrium points. A similar analysis with another foil profile will be presented in a later discussion.

Fig.4.12 shows the first polar plot obtained, where different boom angles β_b were considered for a TWS fixed at 14kn. An important fact to note at this point is that, because the boat is capable of reaching such high velocities, the AWA will factually remain low ($[12.6, ..., 17][°]$) over the whole range of TWA studied here when optimal boat speeds are considered. This, as stated in Chapter 3.2, further justifies the use of the double-skinned mainsail.
The results for $\beta_b = 0[°]$ clearly show that a large range of AWA can already be covered with high boat velocities achieved without any boom setting. This behaviour is indeed very different from traditional monohulls that have to deal with way larger AWA. One can clearly see how much of an impact this boom angle has for extremely low AWA, where a loss of more than 40% would be observed if $\beta_b = 6°$ at TWA = $40°$.
On this Figure is also shown the envelope of all boom angles between zero to six degrees.

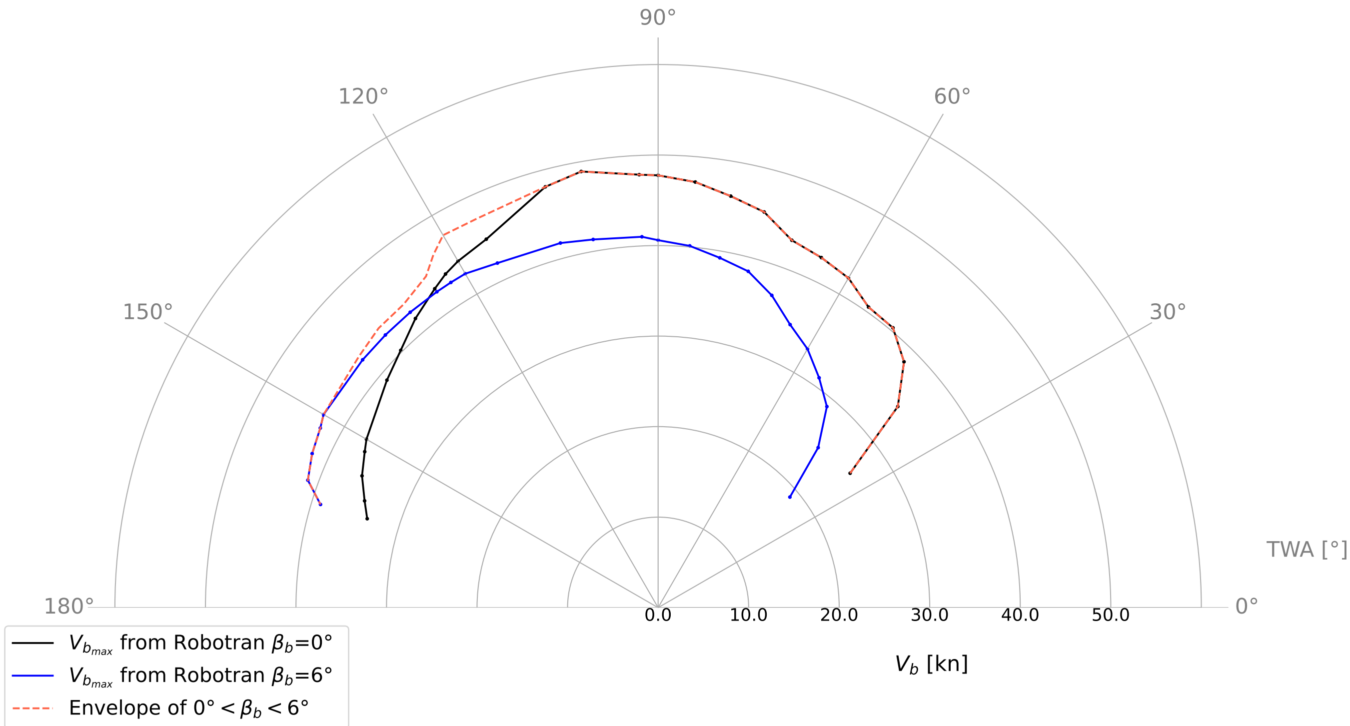

Figure 4.12: Boat velocity V_b $[kn]$: ROBOTRAN prediction for different boom angles β and their envelope

The next Figure (Fig.4.13) shows the comparison of the race data (retrieved from [7]) with the model's results for the $\sim [12, ..., 14]kn$ range of TWS. The envelope that was presented in Fig.4.12 is here represented by the curves each representing a different True Wind Speed. One can observe a fairly good prediction for upwind and downwind values. The mid range values were rarely used during *race 1*, a voluntary choice when looking at the course chosen for the race. The highest values are observed for TWA $= 100°$ and a boat velocity of at most 48.93[kn] = 90.62[kph] leading to an AWA = 16.5°.

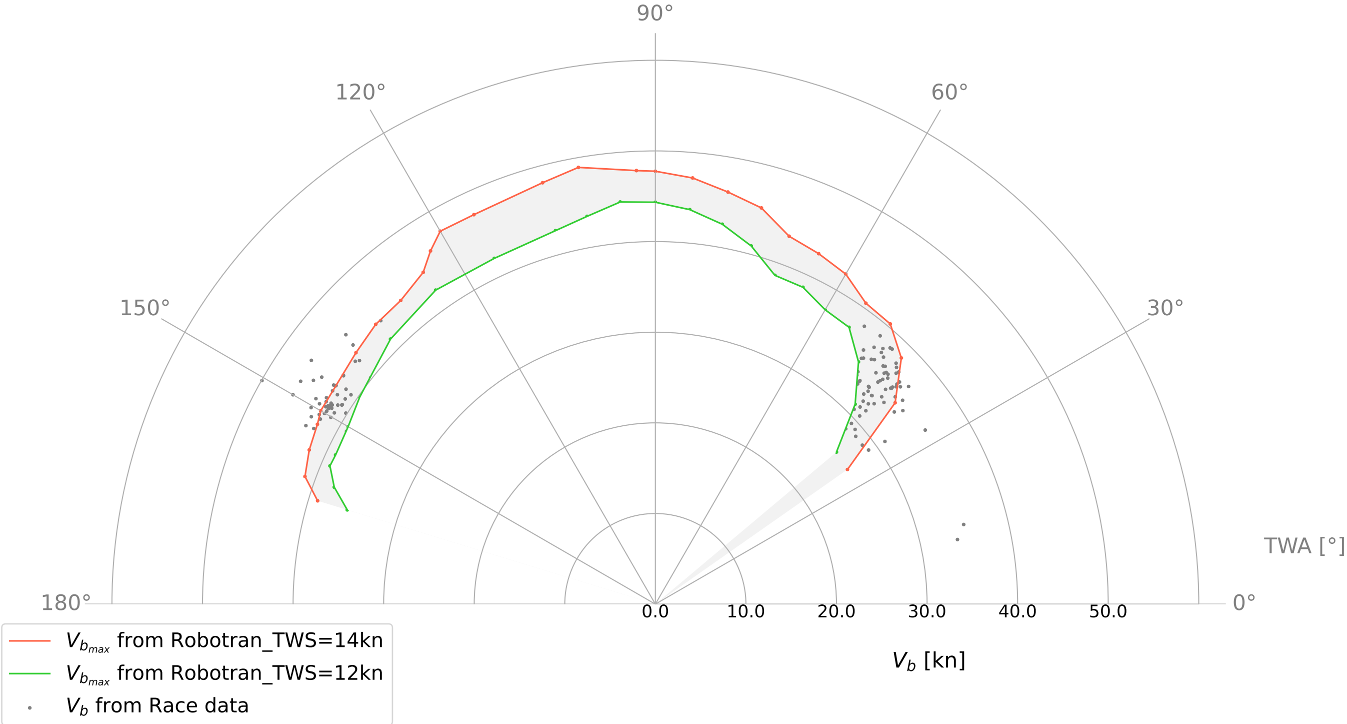

Figure 4.13: Boat velocity V_b $[kn]$: Robotran prediction and race data for different TWS

On Fig.4.14 is shown the velocity made good (VMG) that is, in sailors language, the trade-off between heading and speed: VMG $= V_b \cdot cos(\text{TWA})$
By showing how far upwind the boat would get if sailing at different angles, the graph tells that the peak VMG upwind is at a TWA of about 45°, which seems to fit the data very well. The peak VMG downwind for its part can be seen occurring at a TWA of about 160° which seems to be quite overestimated when compared to race data. This is a direct result of the little underestimation observed in the previous graph.

With the TWS increasing, the optimal upwind TWA decreases and the optimal downwind TWA increases, a rational behaviour that was expected.

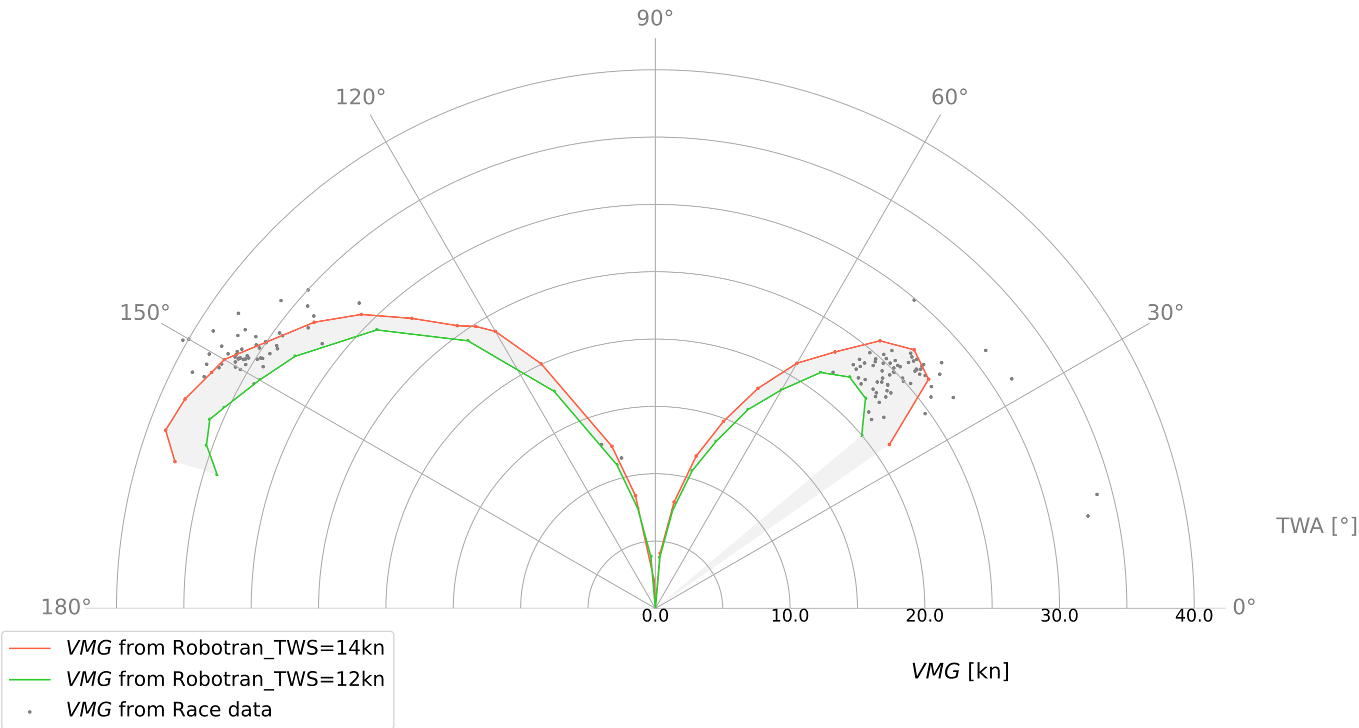

Figure 4.14: Velocity made good VMG $[kn]$: Robotran prediction and race data

On the following Figure 4.15 is shown side by side the heel and the pitch polar diagrams of the boat. On the left diagram, heel predictions are compared to race data. Although fitting rather tolerably the low TWA values, a very large part of the data is underestimated especially at higher TWA. The reality is that given how small the heel angle is thanks to the huge righting moment, every perturbation such a waves or wind gusts felt by the real boat is synonymous of a proportionally 'high' heel variation. This is obviously not taken into consideration by the model. It is interesting to note that while a traditional monohull will be subjected to heel angles between 23 to 33 ° in the same conditions as considered here[18], a decrease in heel would be perceived towards largest values of TWA, when the AWA decreases. Here, again due the very low AWA achieved, no such decrease is seen and the heel is pretty much constant over the entire wind spectrum.

On the right of the Figure, is plotted the pitch angle polar of the boat. Similar behaviours are observed for the wind conditions considered i.e. a large positive pitch for low apparent wind angles, that progressively decrease as the wind shifts more backwards of the boat. The lowest the wind speed the highest the pitch, as expected. An increase in pitch is seen for the TWS = 12[kn] case for TWA values higher that 120[°]. This is believed to be due to the slight decrease in the AWS seen by the boat due to quite sharp slope of V_b in that range, as can be seen on Fig. 4.13.

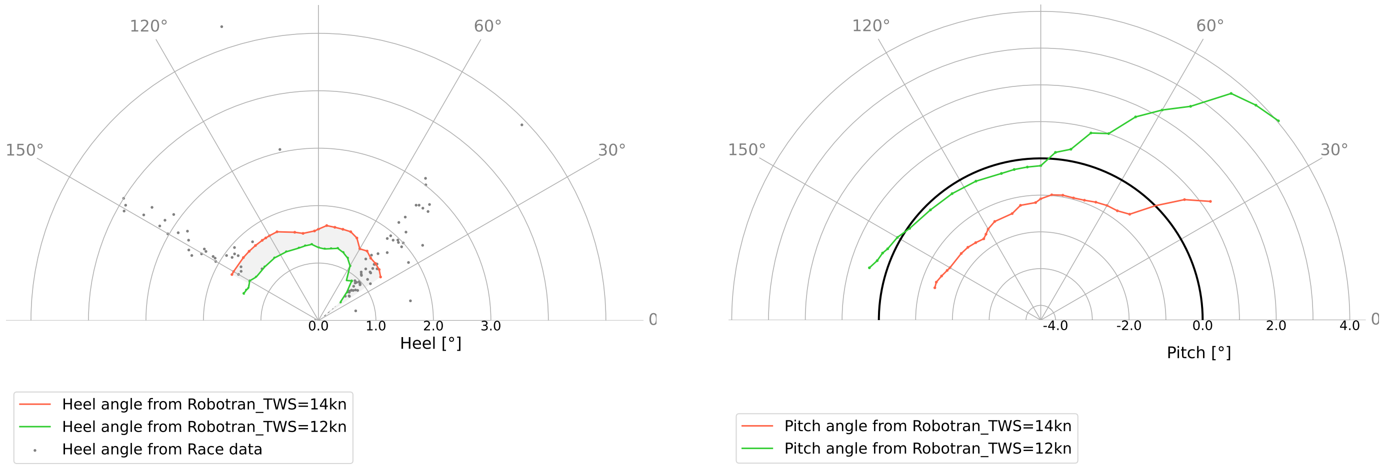

Figure 4.15: Heel [left] and pitch [right] polars: Robotran prediction

On the last figure of this section (Fig. 4.16), the heave travel of the boat is seen to be quite chaotic over the TWA spectrum. The water level plane is set at height of 0.25[m]. Although no entire understanding of this behaviour was made, it is believed that the surface effect on the foil is used by Robotran in order to converge more easily. This behaviour therefore makes those equilibrium positions not quite as continuous between different TWA as desired. But since the goal of these polar plot is only to reflect positions for the maximal achievable speed, it can be said without much doubt that the model will still manage to converge to a stable position during a continuous change in TWA. This configuration however, will not lead to the best achievable speed.

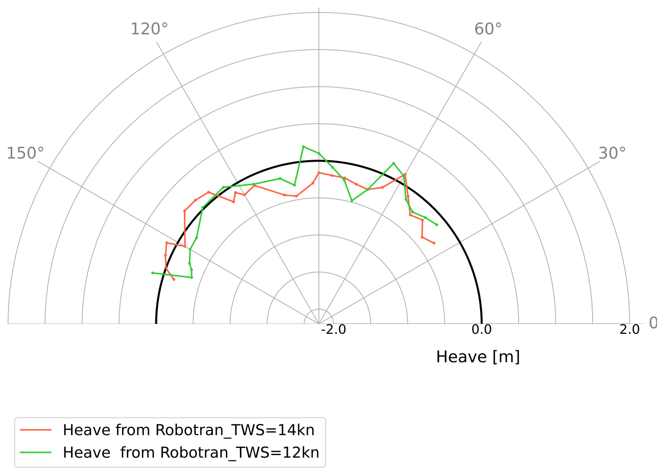

Figure 4.16: Heave $[m]$: Robotran prediction

4.3.2 Impact of the foil profile

Previously in this work was mentioned another foil profile analysis. This analysis intends to point the difference in best top speed achieved with a cambered hydrofoil compared to the symmetric NACA0012 that was studied until now. For this, a GA(W)-1 profile that is a quite thick cambered profile was considered. The results are shown and compared to race data in Fig. 4.17. What can be seen is a quite very neat improvement for low AWA when a lot of lift is required by the foils. For lower AWA though, a lower top speed will be achieved due to the largest drag that the thick GA(w)-1 profile brings. With this in mind, we one more time see that trade-offs will be dominant in the conception of this boat, and that the perfect profile for best overall performance will probably require camber while minimizing drag.

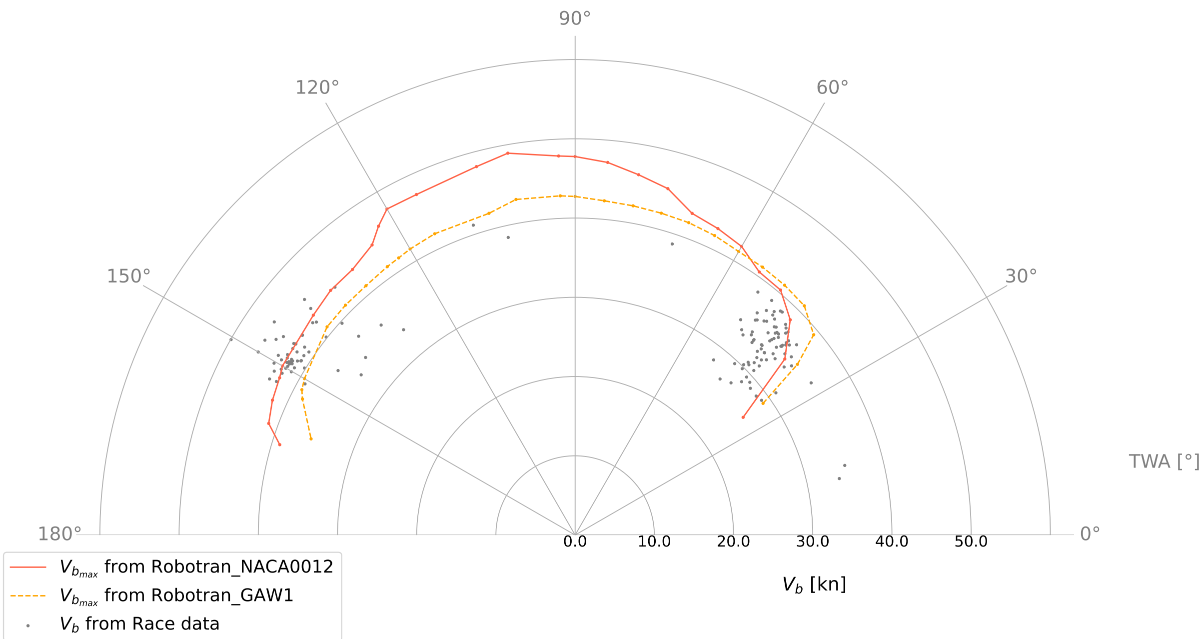

Figure 4.17: Boat velocity V_b $[kn]$: ROBOTRAN prediction and race data for different foil profiles

Conclusion

The aim of this work was to set up a whole-boat simulation model for the AC75 class monohull. The model developed uses relatively basic mathematics with some interesting specific adaptation trials of well-known theories such as the Panel Method or Prandtl Lifting Line. With the aim to still bear significant and usable results, the implementation of those models in ROBOTRAN has proven, through the validation case, that it makes an already very powerful tool for prediction results and parametric analyses. Essential boat behaviours have been depicted and thrilling outputs have been presented, surpassing most of largely used *commercial* Velocity Prediction Programs.
This simulation model allows to dive in the designing process but also to gain understanding of such advanced and puzzling technologies.

As seen through this work, the free surface effect has proven to be a quite very sensitive issue in the case of fully foiling sailboats that, by nature, are much less stable than motorboats. The modelling of this effect presented in this work is believed to be sufficiently realistic for this kind of application but should, for the sake of the argument, be subjected to experimental correlations or more advanced numerical methods that would include the particular case of a tilted foil with respect to the water surface.

The sails model, deemed to be very precise for standard racing sails, has proven to be a great template for the task considered. It should nevertheless be remembered that the sails coefficients were arbitrarily fitted to reach a suggested lift coefficient of 2.2. A more realistic model, once again based on more reliable figures, should help to decrease the uncertainties that come with the current one.
The same can be said of the hull's hydro and aerodynamic behaviours, both having a huge impact on the transition state to foiling as well as being the major component of drag. More data would lead to a possible in-depth analysis of the lift-off phase of the boat, a critical stage during racing events.

Finally, a more extensive use of ROBOTRAN should be envisioned in order to fully benefit from all the assets of the software. Dynamic analyses performed on boat manoeuvers such as the rudder action impact on ride height, the effect of wind gusts or sudden wind angle alterations would provide very worthwhile results.

Bibliography

[1] Norberg D. Uss high point, a hydrofoil patrol boat. *Naval History Heritage Command*, 1963.

[2] Annuario V. photo. Liberty shipyard completes third admiral 250 hydrofoil. *CFF News*, July 2017.

[3] Souppez J-B. et al. Hydrofoil configurations for sailing superyachts: Hydrodynamics, stability and performance. 2019.

[4] Royal New Zealand Yacht Squadron and Circolo Della Vela Sicilia. AC75 Cass Rules v1.28. 2021.

[5] Parkin B. R. Perry B. Wu T.Y. Pressure distribution on a hydrofoil running near the water surface. *CalTech Report 47-2*, 1955.

[6] Faltinsen O. M. *Hydrodynamics of High-Speed Marine Vehicles*. Cambridge University Press, 1990.

[7] Ac2021 public race data. `https://ac36.herokuapp.com/stats_app`. Accessed: 2022-04-01.

[8] Hydrofoiling history. `http://www.hydrofoil.org/history.html`.

[9] Goss N. Confirmed: 36.6 knots according velocitek prostart. `http://sailinganarchy.com/2014/05/14/thats-the-goss/`, May 2014.

[10] Chisnell M. Of Lifting Surfaces. *Sailing World winter 21*.

[11] Dewavrin J. *Design of a Cruising Sailing Yacht with an Experimental Fluid Dynamics Investigation into Hydrofoils*. 2018.

[12] Borba Labi G. *Velocity Prediction Program Development for Hydrofoil-Assisted Sailing Monohulls*. 2019.

[13] Horel B. System-based modelling of a foiling catamaran. *Ocean Engineering 171 (2019) 108–119*, 2018.

[14] Besana G. Computational methods for hydrofoil design a composite analysis using panel code and rans. 2015.

[15] Hui Liang et al. A lifting line theory for a three-dimensional hydrofoil. *J. Marine Sci. Appl. (2011) 10: 199-205*, 2011.

[16] Ni Zao et al. Performance of a hydrofoil operating close to a free surface over a range of angles of attack. *International Journal of Naval Architecture and Ocean Engineering*, 2020.

[17] Xing Tao et al. Numerical study of high-lift hydrofoil near free surface at moderate froude number. *Journal of Hydrodynamics, 2020, 32(1): 44-53*, 2020.

[18] Fossati F. *Aero-Hydrodynamics and the performance of sailing yachts.* Polipress - Politecnico di Milano, 2009.

[19] Masuyama Y. and Fukasawa T. Tacking simulations of sailing yachts with new model of aerodynamic force variation. 2008.

[20] ORC Rating Systems and IMS (International Measurement System). Offshore Racing Congress VPP Documentation. 2021.

[21] Kerwin J.E. *A velocity prediction program for Ocean Racing Yachts.* Rep 78-11 MIT, 1978.

[22] *Brief history of the Offshore Racing Congress.* `https://www.orc.org/index.asp?id=65`. Accessed: 2022-05-19.

[23] Joel Perez Osses Carlos Reusser. *Modern Ship Engineering, Design and Operations.* IntechOpen, 2021.

[24] Winckelmans G. *Travail MECA 2323 : Méthode des panneaux pour l'écoulement autour de profils aéerodynamiques, aussi en effet de sol.* 2010.

[25] Daskovsky M. *The hydrofoil in surface proximity, theory and experiment.* 1999.

[26] Airfoil tools: Naca 0012 airfoils. `http://airfoiltools.com/airfoil/details?airfoil=n0012-il`.

[27] Poncelet A. Docquier N. and Fisette P. *ROBOTRAN: a powerful symbolic generator of multibody models.* Mechanical Sciences, 4(1):199–219, 2013.

[28] *Robotran symbolic generator of multibody models.* `https://www.robotran.be/docs/documentation/`.

[29] T. Demeester J. Degroote A. Bagué, E. Lataire. Dynamic stability analysis of a hydrofoiling sailing boat using cfd. 2019.

[30] Dr. Werner Rheinboldt. *Zur Numerik dynamischer Systeme (english).* Technische Universität München Universitätspresse, 2009.

[31] Mark Drela. *Flight Vehicle Aerodynamics.* The MIT Press, 2014.

[32] *The flying technology of the ac75.* https://www.sailingworld.com/story/racing/flying-technology-of-the-ac75/. Accessed: 2022-7-23.

[33] Version v5: Analysis of ac75 flight parameters by jean sans. http://www.experts-yachts.fr/images/AMERICA_CUP_2020/GBR__V5_AC_75_NZ-12_05_2019_JS_RL.pdf.

Appendix A

Nomenclature of the sailboat

This appendix aims at giving a clear understanding of the nomenclature necessary to understand the sails VPP model computation scheme. It has purposefully been separated from the nomenclature to keep the latter easy to use.

δ_{CEH}	CEH offset
BAS	Distance between mainsail foot and hull
CE	Efficiency coefficient
E	Mainsail foot girth
eff span corr	Corrected effective span of sail set
fcdj	Jib fraction of parasitic drag
ftj	Jib foot parameter, jib reef parameter
HB	Mainsail head girth6
HBI	Height between rig base and waterline
h_{eff}	Sail set / rig effective height
IG	Jib hoist height
J	Jib's foot girth
JGL	Jib quarter span girth
JGM	Jib half span girth
JGU	Jib three quarters span girth
JGT	Jib seven eights span girth
JH	Jib head girth
LP	Distance, measured perpendicular to the luff, from the luff to the clew point of jib
MGL	Mainsail quarter span horizontal length
MGM	Mainsail half span horizontal length
MGU	Mainsail three quarters span horizontal length
MGT	Mainsail seven eights span horizontal length
ROACH	Parameter indication how triangular a sail is

Table A.1: non - essential sailing nomenclature

Appendix B

Details of computation scheme for the sails VPP

B.0.1 Dimensions, standardised area and center of effort

This section aims to give more explanations on the computations behind the reference area of the mainsail and the jib. For the main sail, the foot girth (E), head girth (HB) and main sail span (P) are used for the discretisation in trapezoids. Let's note that the span, P, is computed knowing the foot girth and the mainsail luff length (LL) that is set by the rules at 26750 mm. The quarter/ half/ three quarters/ seven eights main span horizontal length (respectively MGL/ MGM/ MGU/ MGT) are also of use and those are all specified for a certain main sail span in the 36th America's cup class rules [4]. All except for MGT, which has been determined by taking the mean between the head girth and the three quarters main span horizontal length. The dimensions of interest are indicated in figure 3.4 where MGL, MGM and MGU are respectively identified by the 25%, 50%, 75% leech point.
Concerning the jib, there are only two dimensions that will be used to discretise its area and it is the luff length (LL) and LP,the distance from clew point to luff and perpendicular to the luff line. Together they determine all other dimensions. Let's note that LP has a dictated value of 7.050m. From there it is possible to retrieve JGL, JGM, JGU, JGT which are respectively the $\frac{1}{4}$,$\frac{1}{2}$, $\frac{3}{4}$, $\frac{7}{8}$ leech points and JH,the jib's head girth. Again, the rules do not specify JGL and JGT the $\frac{1}{4}$ and $\frac{3}{4}$ leech points dimension and an arithmetic mean between the specified dimensions has been used each time to determine the missing values. The main dimensions of the jib can be identified on figure 3.3 where JGM, JGU and JH are respectively called 50% leech point, 75% leech point and head girth.

With those dimensions it is possible to compute the mainsail standardised area using the following set of equations:

$$MGMH = \frac{P}{2} + \frac{MGM - \frac{E}{2}}{P} \cdot E \tag{B.1}$$

$$MGLH = \frac{MGMH}{2} + \frac{MGL - \frac{E+MGM}{2}}{MGMH} \cdot (E - MGM) \tag{B.2}$$

$$MGUH = \frac{MGMH + P}{2} + \frac{MGU - \frac{MGM}{2}}{P - MGMH} \cdot MGM \tag{B.3}$$

$$MGTH = \frac{MGUH + P}{2} + \frac{MGT - \frac{MGU}{2}}{P - MGUH} \cdot MGU \tag{B.4}$$

$$\begin{aligned} Area_{mainsail} = {} & \frac{MGL + E}{2} \cdot MGLH + \frac{MGL + MGM}{2} \cdot (MGMH - MGLH) \\ & + \frac{MGM + MGU}{2} \cdot (MGUH - MGMH) \\ & + \frac{MGT + MGU}{2} \cdot (MGTH - MGUH) + \frac{MGT + HB}{2} \cdot (P - MGTH) \end{aligned} \tag{B.5}$$

The roach of the mainsail is also computed. It is a parameter that determines how triangular the mainsail is. A small roach means that the leech, back side of the sail, is very straight and thus the shape of the sail is triangular. A big roach means that the leech is curved and we thus have to compute the added area. This is done with those 2 equations:

$$Upper_{\frac{3}{4}} = \frac{P}{8} \cdot (MGL + 2MGM + 1.5MGU + MGT + 0.5HB) \tag{B.6}$$

$$ROACH = \frac{\frac{Upper_{\frac{3}{4}}}{0.375 \cdot P \cdot MGL} - 1}{0.844} \tag{B.7}$$

Where $Upper_{\frac{3}{4}}$ is the upper $\frac{3}{4}$ part of the mainsail to avoid any influence of the gap at the foot of the sail in the computations.
The jib's standardised area is computed, as explained earlier thanks to LL and LP that determine all the other dimensions:

$$Area_{jib} = 0.1125LL \cdot (1.445LP + 2JGL + 2JGM + 1.5JGU + JGT + 0.5JH) \tag{B.8}$$

B.0.2 Blanketing factors for the combined sails characteristics

In the case of the ac75 the blanketing factors have the following expression for the main sail:

$$b_k(AWA) = \begin{cases} 1 & \text{if } AWA \leq 90^\circ \\ 1 - 0.5f_m[\,1 - 1.5\frac{AWA-135}{45} - 0.5\frac{AWA-135}{45}^3\,] & \text{if } 90^\circ < AWA \end{cases} \tag{B.9}$$

where f_m is a non zero factor in case the ship has a mizzen staysail which is not the case here. The blanketing factor of the main sail is thus always equal to unity. This implies that no matter at what angle the wind blows, the main sail will always be used at its full potential. This seems logical given the crucial part the main sail plays.

Concerning the jib, the blanketing factors has the following behaviour:

$$b_k(AWA) = \begin{cases} 1 & \text{if } AWA \leq 135° \\ 1 - f_j[\frac{AWA-135}{45}] & \text{else} \end{cases} \tag{B.10}$$

Where $f_j = \frac{A_{jib} - min(A_{jib}, A_{fore})}{A_{jib}}$ is equal to one if the ship does not possess a foresail because $A_{fore} = 0$. The blanketing factor abruptly drops from 1 to 0 at a wind angle of $135°$ because it gets totally shielded by the main sail. This is rarely the case because the ac75 has a close hauled point of sail most of the time. The only time where this is not valid is when the foil boat is running downwind. This is a very particular case in sailing and is almost never used in America's cup racing.

Some adjustments are also made to the total center of effort height. The center of effort height of a sailboat is reduced when the jib area is reduced or reefed. It decreases up to a minimum of 5% of the hoist height of the jib (IG) as can be seen in the next formula:

$$Z_{ce} = Z_{ce} \mid_{ftj=1} - \delta_{CEH} \tag{B.11}$$

$$\delta_{CEH} = (1 - ftj) \cdot 0.05 \cdot IG \tag{B.12}$$

The influence of sail plan geometry is calculated to derive a corrected effective span coefficient *eff span corr* . This takes into account several shape and dimension parameters that will determine effective rig height:

$$effspancorr = 1.1 + 0.08 \cdot (ROACH - 0.2) + \frac{1}{2} \cdot (0.68 + 0.31 \cdot fractionality + 0.075 \cdot overlap) \tag{B.13}$$

where *fractionality* is $\frac{I}{P+BAS}$, I is the measured rig height and BAS is the distance between the boom and the hull. This distance is equal to zero due to the fact that having a gap there reduces the mainsail's efficiency. *Overlap* is $\frac{LP}{J}$ where J is the jib's foot girth.

An additional modification to the effective span coefficient is made as the AWA becomes wider. Indeed, at higher AWA, the sealing between the jib and the hull is lost and the sail thus loses efficiency. This is reflected through the following modification on *eff span corr* where $x = \frac{AWA-60}{30}$:

$$cheff_{upwind} = effspancorr \cdot (0.8 + 0.2 \cdot b_e) \tag{B.14}$$

$$b_e(AWA) = \begin{cases} 1 & \text{if } AWA \leq 30° \\ \frac{1}{2}(1 - 1.5 \cdot x + 0.5 \cdot x^3) & \text{if } 30° < AWA < 90° \\ 0 & \text{if } 90° \leq AWA \end{cases} \tag{B.15}$$

After all these steps the rig's effective height can be computed by taking the product of $cheff_{upwind}$ and the highest point above the waterplan:

$$h_{eff} = cheff_{upwind} \cdot (P + HBI) \tag{B.16}$$

With , as stated before, P the mainsail span and HBI the height between the rig base and the water level. From there an efficiency coefficient *CE* is determined, comprised of the parasitic drag coefficient *KPP* and the induced drag coefficient that itself is proportional to the lift squared:

$$CE = KPP + \frac{A_{ref}}{\pi \cdot h_{eff}} \tag{B.17}$$

where $C_{D,i} = \frac{C_{L,max}^2 \cdot A_{ref}}{\pi \cdot h_{eff}}$ is the induced drag of the total sail set.

To close the appendix, the last two empirical parameters are discussed. Fcdj is the fraction of parasitic drag due to the jib and fcdmult is a coefficient that symbolises the fact that when the flat parameter decreases, an increase of the induced drag is observed with respect to the square of the lift. fcdmult is thus function of the flat parameter.

flat [-]	fcdmult [-]
0.1	1.06
0.2	1.06
0.3	1.06
0.4	1.06
0.5	1.06
0.55	1.06
0.6	1.055
0.65	1.048
0.7	1.035
0.75	1.020
0.8	1.008
0.85	1.002
0.9	1.00
0.95	1.004
1	1.06

Table B.1: multiplier to drag coefficient to materialise the not perfectly linear behaviour of $C_{D,i}$ in function of C_L^2

NB: Twist function

In order to reflect the fact that as sails are de-powered the centre of effort height moves lower a "twist function" was introduced, relating the center of effort height to the amount of *flat* used. The extent of the centre of effort lowering was determined from wind tunnel test results, which showed that this effect was proportional to the fractionality I/(P + BAS) ratio.[20]

$$ZCE = ZCE\mid_{flat=1} \cdot [1 - 0.203\,(1 - flat) - 0.451\,(1 - flat)(1 - frac)] \tag{B.18}$$

This was determined from wind tunnel testing with *frac* the relative positions of the mainsail head and the jib head.

Appendix C

Pressure coefficients - "biplane image" panel method for different AoA, at h/b=0.7, NACA0012, 350panels

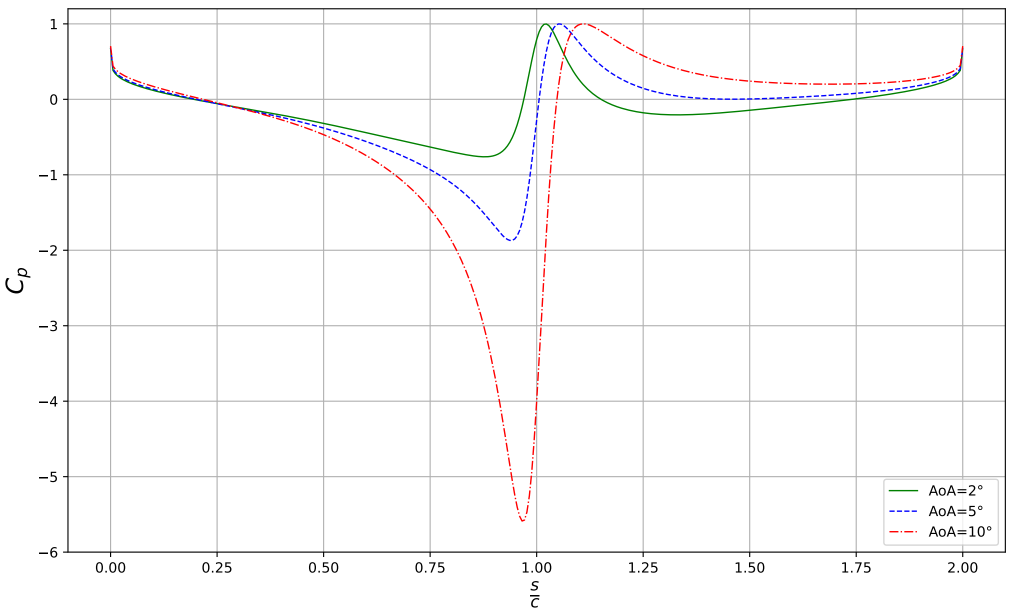

Figure C.1: Pressure coefficients for different AoA, $\frac{h}{c} = 0.7$, NACA0012, 500panels

Appendix D

Biplane Lifting Line method from Section 3.3.2

D.1 Classic Lifting Line - detailed calculations

With $\Gamma(y)$ the circulation around the aerodynamic profile located at y and by continuity of vortex tubes, a vortex sheet must be shed as depicted on Fig.3.19 & D.1.

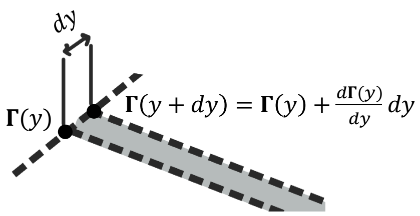

Figure D.1: Shed vortex sheet

D.2 Biplane Lifting Line - detailed calculations

The distribution of the downwash velocity $-w(y)$ is, again, obtained from the Biot-Savart velocity induced by the wake and its image as :

$$\begin{aligned}
-w(y) &= \frac{1}{4\pi}\int_{-b/2}^{b/2}[\frac{1}{y-y'} + \frac{cos(\beta+2\delta)}{r}]\frac{d\Gamma(y')}{dy'}\,dy' \\
&= \frac{1}{4\pi}\int_{-b/2}^{b/2}[\frac{1}{y-y'} + \frac{cos(\beta+\delta)cos\delta - sin(\beta+\delta)sin\delta}{r}]\frac{d\Gamma(y')}{dy'}\,dy' \\
&= \frac{1}{4\pi}\int_{-b/2}^{b/2}[\frac{1}{y-y'} + \frac{(y-y')cos^2\delta - (2h+(y+y')sin\delta)sin\delta}{(2h+(y+y')sin\delta)^2 + ((y-y')cos\delta)^2}]\frac{d\Gamma(y')}{dy'}\,dy' \qquad \text{(D.1)}
\end{aligned}$$

with the same change of variable as for the case without tilt, we get :

$$\begin{aligned}
&-\frac{w(\theta)}{U_\infty} = \frac{1}{2\pi}\sum_n nB_n\ [\ \frac{\pi sin(n\theta)}{sin(\theta)} \\
&+ \int_0^\pi \frac{(cos\theta' - cos\theta)(cos\delta)^2 - (\frac{2h}{b/2} + (cos\theta' + cos\theta)sin\delta)sin\delta}{(\frac{2h}{b/2} + (cos\theta' + cos\theta)sin\delta)^2 + ((cos\theta - cos\theta')cos\delta)^2}\cdot cos(n\theta')\,d\theta'\ \ ] \qquad \text{(D.2)}
\end{aligned}$$

UNIVERSITÉ CATHOLIQUE DE LOUVAIN
École polytechnique de Louvain
Rue Archimède, 1 bte L6.11.01, 1348 Louvain-la-Neuve, Belgique | **www.uclouvain.be/epl**